IGS

Article

Corresponding author: Yota Sato;
Email: yota.sato@jamstec.go.jp

Modelling seasonal fluctuations and aspect characteristics of ice-cliff melt on the debris-covered Trakarding Glacier, Rolwaling Valley, Nepal Himalaya

Yota Sato[1,2] (ID), Pascal Buri[3,4] (ID), Marin Kneib[3,5], Evan S. Miles[3],
Sojiro Sunako[6] (ID), Tika R. Gurung[7] (ID), Akiko Sakai[2] (ID), Francesca Pellicciotti[3,8]
and Koji Fujita[2] (ID)

[1]Research Institute for Global Change (RIGC), Japan Agency for Marine-Earth Science and Technology (JAMSTEC), Yokohama, Japan; [2]Graduate School of Environmental Studies, Nagoya University, Nagoya, Japan; [3]Swiss Federal Institute for Forest, Snow and Landscape Research (WSL), Birmensdorf, Switzerland; [4]Geophysical Institute, University of Alaska Fairbanks, Fairbanks, USA; [5]Institute of Environmental Engineering, ETH Zurich, Zurich, Switzerland; [6]Snow and Ice Research Center, National Research Institute for Earth Science and Disaster Resilience (NIED), Nagaoka, Japan; [7]International Center for Integrated Mountain Development (ICIMOD), Kathmandu, Nepal and [8]Department of Geography, Northumbria University, Newcastle, UK

Abstract

Ice cliffs on debris-covered glaciers act as melt hotspots that considerably enhance glacier ablation. However, studies are typically limited in time and space; glacier-scale studies of this process of ice cliff melt are rare, and their varying seasonal energy balance remains largely unknown. In this study, we combined a process-based ice cliff backwasting model with high-resolution (1.0 m) photogrammetry-based terrain data to simulate the year-round melt of 479 ice cliffs on Trakarding Glacier, Nepal Himalaya. Ice cliff melt accounted for 26% of the mass loss of the glacier from October 2018 to October 2019, despite covering only 1.7% of the glacier surface. The annual melt rate of ice cliffs was 2.7 cm w.e. d^{-1}, which is 8–9 times higher than the sub-debris melt rate. Ice cliff melt rates were significantly controlled by their aspects, with south-facing ice cliffs showing a melt rate 1.8 times higher than that of north facing ones. The results revealed that the aspect dependence of ice cliff melt rate was amplified in winter and decreased/disappeared toward the monsoon season. The seasonal changes in melt characteristics are considered to be related to variations in direct shortwave radiation onto the cliff surface, which are dependent on changes in solar altitude and monsoonal cloud cover.

1. Introduction

Glaciers in High Mountain Asia, including the >10% with debris-covered surfaces (Herreid and Pellicciotti, 2020), have been losing mass during recent decades (e.g. Brun and others, 2017; Shean and others, 2020; Miles and others, 2021). A thick debris mantle insulates the underlying ice, whereas a thin debris layer tends to enhance ice ablation (e.g. Østrem, 1959; Fyffe and others, 2014; Collier and others, 2015). It has been suggested that the insulating effect of debris reduces glacier mass loss; however, several studies have reported that debris-covered glaciers show comparable or greater thinning rates relative to clean glaciers, even when controlling for elevation biases (e.g. Nuimura and others, 2012; Lamsal and others, 2017; Brun, 2019). This phenomenon is known as the debris-covered anomaly (Pellicciotti and others, 2015; Salerno and others, 2017) and is generally attributed to a combination of melt enhancement and ice dynamics (e.g. Rounce and others, 2021). Previous studies have suggested that ice cliffs can cause local enhancement of debris-cover glacier surface melt rates (e.g. Sakai and others, 1998; Buri and others, 2021; Miles and others, 2022), contributing to the debris-cover anomaly, but the glacier-wide contribution of cliffs to mass balance is known for only very few sites (e.g. Buri and others, 2021).

Previous studies have attempted to quantify ice cliff backwasting (horizontal retreat) and melt rate (perpendicular ice loss) using in situ measurements (e.g. Sakai and others, 1998; Steiner and others, 2015; Anderson and others, 2021a), terrestrial photogrammetry (e.g. Brun and others, 2016; Watson and others, 2017a; Kneib and others, 2022), airborne remote sensing (e.g. Brun and others, 2018; Mishra and others, 2022), and energy balance modelling (e.g. Han and others, 2010; Steiner and others, 2015; Buri and others, 2016a, b). In particular, the widespread use of Unoccupied/Uncrewed Aerial Vehicles (UAVs) and Structure from Motion (SfM) technology has dramatically advanced ice cliff studies (e.g. Brun and others, 2018; Immerzeel and others, 2014; Mishra and others, 2022;

Zhao and others, 2023). Although the digital elevation model (DEM)-differencing approach can potentially derive precise mass loss of an ice cliff, this approach requires repeated photogrammetric surveys and consideration of ice dynamics, either directly or through mass conservation approaches that require measuring/modelling physical parameters (ice thickness and horizontal/vertical velocity distributions; Brun and others, 2018; Mishra and others, 2022; Zhao and others, 2023). This approach also lacks the temporal resolution to explain how ice cliffs fluctuate between the initial and subsequent timing of aerial photogrammetric surveys and provides only the total amount of melt. Other studies have developed energy balance models to quantify ice cliff mass loss (e.g. Sakai and others, 1998; Reid and Brock, 2014). Recent studies have combined UAV-based high-resolution terrain data with energy balance modelling (e.g. Steiner and others, 2015; Buri and others, 2016a), expanding the potential for estimating melt patterns on the highly heterogeneous surfaces of ice cliffs. The energy balance approach can extend our knowledge of the temporal/sub-seasonal variability of ice cliff ablation and its mechanisms (i.e. the relationship with meteorological factors and ablation characteristics), rather than simply deriving mass loss. Such models have been shown to adequately quantify ice cliff melt at fine temporal scales and to be transferable across different climatic settings (Kneib and others, 2022). Buri et al. (2021) first applied an energy balance model for ice cliffs that takes into account the cliff morphological changes to the catchment scale. Although these authors succeeded in quantifying the contribution of ice cliff mass loss to four glaciers in the Langtang Valley of the Nepal Himalaya, glacier-scale applications of ice cliff energy balance models are rare. Hence, the transferability of such a model to other regions with different climatic conditions needs to be confirmed. The reason why such studies are limited is because the application of an ice cliff energy balance model at the glacier scale requires high-resolution topographic data and an ice cliff inventory covering the entire debris-covered area to reconstruct the heterogeneous glacier surface. In addition, meteorological data (especially incoming shortwave and longwave radiation) over debris-covered glaciers at high altitude and the temperature characteristics of the supraglacial debris are also essential to force such process-based models. Furthermore, because previous studies focused on only short-term (Sakai and others, 1998; Buri and others, 2021), the monthly fluctuations in ice cliff geometry and energy balance, and their relationship to morphological/energy-balancing characteristics on glacier-wide and annual scales, remain largely unknown.

In this study, we combine high-resolution aerial photogrammetric data and a process-based energy balance model to (1) characterise the monthly melt rate of ice cliffs, (2) estimate the annual ice cliff mass loss and its contribution to the glacier mass balance, and (3) quantify the contribution of different energy fluxes at the cliff surface on debris-covered Trakarding Glacier in the eastern Nepal Himalaya.

2. Study site, data and methods

2.1. Study site

Debris-covered Trakarding Glacier (27.9°N, 86.5°E) is located in Rolwaling Valley in the eastern Nepal Himalaya (Fig. 1a). This glacier spans elevations of 4530–6670 m above sea level (a.s.l.). The terminus of Trakarding Glacier is Tsho Rolpa, one of the largest glacial lakes in Nepal and a site of glacial lake hazard management. Trakarding Glacier covers an area of 8.21 km^2, and

41% of its surface is covered by debris (Herreid and Pellicciotti, 2020). The glacier accumulates mass mainly from avalanches from the southeastern rock wall. Measured debris thickness on the glacier ranges from a few centimetres to ∼70 cm, with the maximum thickness being observed near the terminus. Trambau Glacier is situated above Trakarding Glacier, and the two glaciers have been disconnected since 1970 (Fig. 1a). Therefore, previous studies have tended to consider these glaciers together as the 'Trambau–Trakarding glacier system' (Sunako and others, 2019). We have been conducting in situ measurements on Trakarding Glacier since May 2016 using meteorological instruments and ablation stakes. We also conducted aerial photogrammetric surveys in October 2018 and October 2019 (Sato and others, 2021; Section 2.2), which defined the period of interest for the model simulation. This study investigates ice cliffs over a 2.93 km^2 area of Trakarding Glacier (Fig. 1a, b, and d), covering most of the debris-covered part. We modified glacier outlines obtained from the GAMDAM glacier inventory (Nuimura and others, 2015; Sakai, 2019) to match the glacier width and terminus positions in October 2018.

2.2. Terrain data and ice cliff inventory

We used high-resolution photogrammetry-based terrain data and an ice cliff inventory to compute cliff melt using an energy balance model (Section 2.3). Details of the datasets have been described by Sato and others (2021). The photogrammetric datasets were obtained on 18 October 2018 and 18–19 October 2019. We used a helicopter in 2018 and a fixed-wing UAV in 2019. These photogrammetric datasets covered most of the debris-covered area of the glacier. We generated high-resolution orthoimages and DEMs with 0.2 m resolution (hereafter SfM-orthoimages and SfM-DEMs) using the SfM software package Agisoft Metashape Professional Edition version 1.5.1. We conducted kinematic GPS surveys on-/off-glacier, and vertical uncertainties of these SfM-DEMs were estimated at ±1.82 m in 2018 (26,142 validation points) and ±2.35 m in 2019 (based on 8,790 points), respectively. From these SfM-orthoimages and SfM-DEMs, we manually delineated all ice cliffs and supraglacial ponds on Trakarding Glacier using ArcGIS. We found 481 ice cliffs in the 2018 orthoimages, covering an area of 1.38×10^5 m^2 (Fig. 1d). The delineation uncertainty in individual cliff map-view areas (planimetric areas) was assessed by five operators and did not exceed 10% area of the cliff inventories. In addition, with respect to the sensitivity of the inclined area (actual area of ice cliff slope) to the quality of the DEM, the slope angle uncertainty of ±1° does not cause more than ±2% of inclined area changes (Sato and others, 2021).

2.3. Meteorological observations and debris surface temperature estimation

We obtained meteorological data from an automatic weather station (AWS) located beside Trakarding Glacier (4806 m a.s.l.; Fig. 1c and Table 1). Details of the meteorological observations have been described by Sunako et al. (2019) and Fujita et al. (2021). Air temperature, ground surface temperature, wind speed, relative humidity, and upward/downward shortwave radiation were recorded from May 2016 to November 2021. Air temperatures over the debris-covered area were also measured to calculate the temperature lapse rate. Unfortunately, the air temperature stations on the glacier were not operational during the period of interest (October 2018 to October 2019); therefore, we estimated the seasonal temperature lapse rate from air temperatures measured on
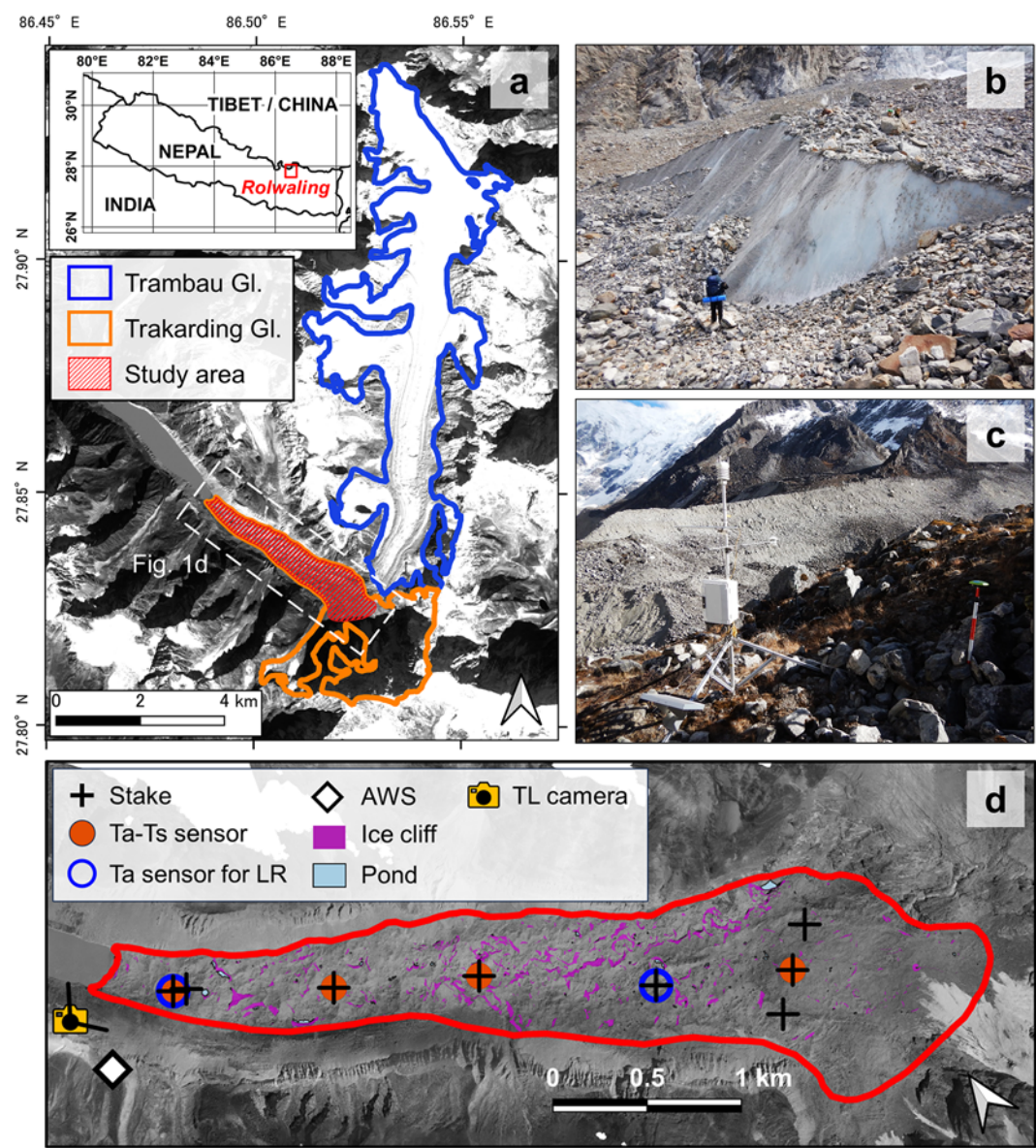
Figure 1. Overview of the Trambau–Trakarding glacier system. (a) Location of the rolwaling region (inset) and outline of Trambau glacier, Trakarding glacier, and the study area; (b) an ice cliff in the debris-covered area; (c) the automatic weather station (AWS) beside Trakarding glacier; and (d) locations of air (t_a) and debris surface (t_s) temperature sensors, AWS, ablation stakes, time-lapse (TL) camera, and ice cliffs. glacier outlines in (a) are from the GAMDAM glacier inventory (Nuimura and others, 2015). Blue circles in (d) are air temperature sensors that were used to calculate the temperature lapse rate (LR; Fig. 2 and Table 1), and orange dots are temperature sensors for air and debris surface (Figs. 3, S1 and Table 1).

Table 1. Details of meteorological instruments on Trakarding Glacier, the locations of which are shown in Fig. 1d. Details of meteorological observations at the AWS have been described by Sunako et al. (2019) and Fujita et al. (2021)

|	Observation	Instrument	Sensor type	Elevation(m a.s.l.)	Precision
AWS	Air temperature (°C)	Capacitance-type temperature sensor	Vaisala WXT520	4806	±0.3 °C
	Relative humidity (%)	Capacitance-type humidity sensor	Vaisala WXT520		±3%
	Wind speed (m s^{-1})	Ultrasonic anemometer	Vaisala WXT520		±0.3 m s^{-1}
	Downward shortwave radiation (W m^{-1})	Pyranometer	Kipp & Zonen CMP3		±10%
	Air temperature with debris surface temperature (°C)	Pt temperature sensor	TPT100	4590, 4628, 4642, 4773	±0.2 °C
	Air temperature for lapse rate (°C)	Thermistor sensor	T&D TR − 52i	4590, 4719	±0.3 °C

the debris-covered area from March 2020 to October 2021 (Figs. 1d and 2, and Table 1). We divided this period into four seasons and calculated the seasonal/hourly temperature lapse rate following Heynen et al. (2016).

To calculate longwave radiation flux from heated debris, it is necessary to estimate the spatiotemporal surface temperature distribution, which we obtained on the basis of correlation with air temperature on the glacier (Foster and others, 2012; Steiner and
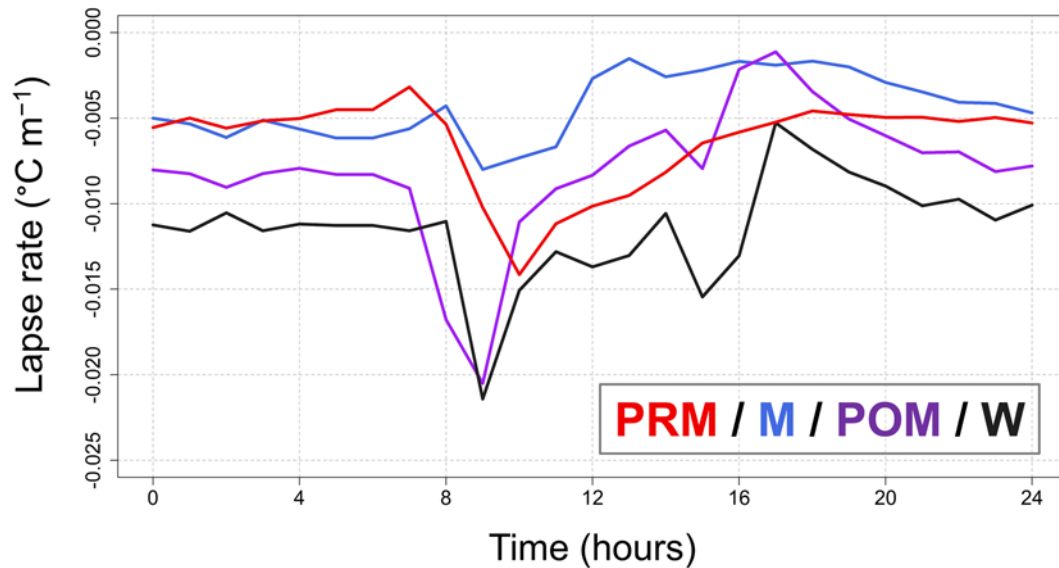
Figure 2. Temperature lapse rates over the debris-covered area of Trakarding glacier in the pre-monsoon (PRM; 1 march to 14 June), monsoon (M; 15 June to 30 September), post-monsoon (POM; 1 October to 30 November), and winter (W; 1 December to 28 February) seasons. The locations of the air temperature sensors are shown in Fig. 1d.
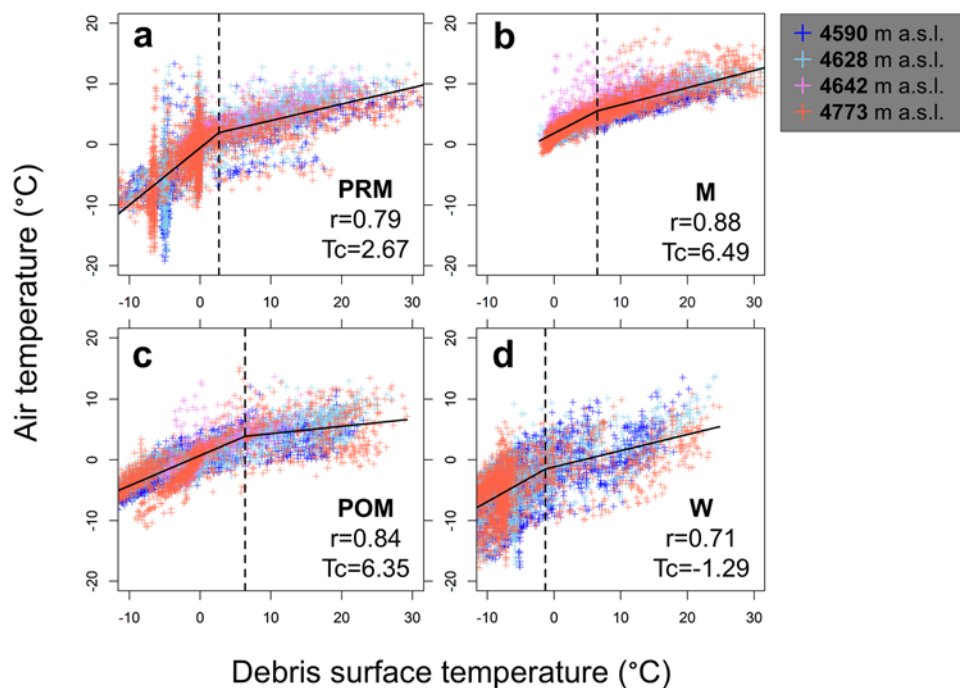
Figure 3. Relationship between air temperature and debris surface temperature in the pre-monsoon (a), monsoon (b), post-monsoon (c), and winter (d) seasons. Different colours indicate different locations (Figs. 1d and S1, and Table 1). Dashed vertical lines represent the threshold temperature (t_c) in the piece-wise regression. Letter 'r' is the mean correlation coefficient between debris surface temperature and air temperature. The time series of air and debris surface temperatures are plotted in Figure S1.

Pellicciotti, 2016). We measured air temperature (1.5 m above ground) and debris surface temperature at the same four locations (Fig. 1d and Table 1). These sensors were installed in May 2016, and they recorded air/debris temperature until November 2017 (Fig. S1). We then applied piece-wise linear regression between air temperature and debris surface temperature (Fig. 3). The air/debris temperature data were classified into four seasons, and the most appropriate piece-wise linear regressions were estimated from all temperature observation sites. Significant correlations were obtained for all seasons (Fig. 3). The resultant empirical equations

were combined with the air temperature lapse rate to estimate the spatial distribution of debris surface temperature.

2.4. Dynamic 3D ice cliff backwasting model

We employed a process-based dynamic 3D ice cliff backwasting model (hereafter; dynamic cliff backwasting model) developed by Buri et al. (2016b) to estimate year-round ice cliff mass loss. A full description of the model has been provided by Buri et al. (2016b), Buri and Pellicciotti (2018), and Buri et al. (2021); therefore, only

a brief summary is provided here. This grid-based model estimates the mass loss of ice cliffs by calculating the hourly energy balance on the cliff surface. The energy balance is calculated as follows:

$$Q_m = I_n + L_n + H + LE \tag{1}$$

where Q_m is the energy flux for cliff surface melt, I_n and L_n are net shortwave and longwave radiation fluxes, H is sensible heat flux, and LE is latent heat flux. Units of all fluxes are in W m^{-2}. Previous studies neglected heat from precipitation and conductive heat flux into the ice cliff surfaces (e.g. Reid and Brock, 2014). We also assume the conductive flux to be negligible when Q_m is positive or zero. In some rare cases the energy balance can be negative, indicating either a non-negligible conductive heat flux or refreezing. In these cases, we treat Q_m as zero in the melt calculation, and we discuss this effect later (Section 4.5).

The dynamic cliff backwasting model uses a high-resolution DEM to calculate radiation fluxes that account for complex cliff slope geometry and debris-covered surface topography. The ice cliff and glacier surface topography were reconstructed from SfM-DEM-2018 (Section 2.2), and the valley/mountain topography surrounding the calculation area was obtained from ASTER-GDEM3. The SfM-DEM was resampled to 1.0 m resolution owing to the computational cost. Then, two ice cliffs were excluded from the simulation because they were too small and contained only a few grid cells, resulting in 479 ice cliffs being used as model input. These topographic datasets allowed the calculation of sky- and debris view angles for each grid cell on the cliff surface to estimate net radiation. Incoming shortwave radiation consists of direct shortwave radiation (I_s), diffuse shortwave radiation from the sky (D_s), and incoming shortwave radiation reflected from terrain (D_t). The incoming shortwave radiation observed at the AWS was split into I_s and D_s following Reindl et al. (1990). This approach uses a clearness index, which is the ratio of incoming shortwave radiation at the AWS to theoretical extraterrestrial solar radiation, which has been used in previous cliff modelling studies (Han and others, 2010; Reid and Brock, 2014). Incoming longwave radiation comprises longwave radiation from the sky (L_s) and from surrounding debris (L_d). These longwave fluxes were modelled using the Stefan–Boltzmann relation forced by air and debris surface temperature (Section 2.3). Finally, the cliff volume loss (V_{cl}; m^3 w.e.) was calculated as follows:

$$V_{cl} = \frac{Q_m \cdot \Delta t \cdot S}{\rho_i L_f} \tag{2}$$

where Δt is the simulation time step (3600 s), S is a map-view area of ice cliff (m^2), ρ_i is ice density in the debris-covered area (900 kg m^{-3}), and L_f is the latent heat of fusion of ice (334 kJ kg^{-1}).

Furthermore, the dynamic cliff backwasting model incorporates changes in ice cliff geometry associated with its ablation. This allows a realistic long-term energy balance to be calculated for ice cliffs, which are known to morphological change considerably over time (Watson and others, 2017b; Kneib and others, 2021; Sato and others, 2021; Kneib and others, 2022). In our study, we set nine geometry updates over one year. The first geometry update was on 28 February 2018, the end of the winter season, followed by geometry updates on the last day of each month until the end of the simulation period (18 October 2019). The geometry updates consider expansion due to cliff backwasting and shrinkage/burial due to debris slumping. Some ice cliffs were completely buried and disappeared during the simulation period. In this study, the angle at which the ice cliff surface was buried by debris (slope threshold) was set at 35° after some trials comparing model output and observed ice cliff shape at the end of the simulation period

in October 2019 (Sato and others, 2021). As previous studies have reported that the angle of repose for debris mantle varies between 30° and 45° (Sakai and others, 2002; Kraaijenbrink and others, 2016; Moore, 2018; Westoby and others, 2020; Sato and others, 2021), this threshold is considered reasonable. Further detailed model parameters/settings are given in Table S1. This study is the first attempt to apply this dynamic model to an entire glacier on a year-round time scale. When we calculated annual cliff melt rates, the initial/final ice cliff areas largely changed in this dynamic cliff backwasting model. Hence, the daily melt rate of each ice cliff surface (M_d; m w.e. d^{-1}) was defined as follows:

$$M_d = \frac{2\Delta V}{(S_1 + S_2) \cdot \Delta t} \tag{3}$$

where ΔV is the cumulative cliff volume loss in one year (m^3 w.e.), S_1 and S_2 are the initial and final ice cliff areas during the simulation period (m^2), and Δt is the number of days (365 days). In this study, ice cliff melt rate is defined as the rate of vertical ablation at each grid cell.

In the case where ice cliffs are covered in snow, the energy flux on the cliff surface should be used to melt the snow layer without melting the ice cliffs. To determine the effect of snow on ice cliff melt, we examined daily time-lapse photographs taken near the glacier terminus to assess snow cover, obtained using a Brinno TLC200 time-lapse camera that has a 112° field of view (Fig. 1d and S2a–d). Photographs were taken each day at 13:46 (Nepal time, UTC + 5:45) and were used to estimate the number of snow-covered days in each month. We assumed that all ice cliffs had zero melt for an entire day if snow cover was visible at the glacier terminus. We applied the number of snow cover days in the target month (d_{snow}; days) to reduce the monthly ice cliff volume loss ($V_{cl,\,month}$; m^3 w.e.) accounting for snow cover as follows:

$$V_{cl,\,month} = \frac{V_{cl,\,est} \cdot (d_{month} - d_{snow})}{d_{month}}, \tag{4}$$

where $V_{cl,\,est}$ is the monthly ice cliff volume loss without considering snow cover (m^3 w.e.) and d_{month} is the number of days in the target month ($\sim$30 days). Then we defined overestimated ice cliff volume loss ($V_{cl,\,overest}$; m^3 w.e.), that would not have occurred due to the presence of snow as follows:

$$V_{cl,\,overest} = V_{cl,\,est} \cdot \frac{d_{snow}}{d_{month}} \tag{5}$$

2.5. Model validation and sensitivity analysis

The dynamic cliff backwasting model was developed based on studies at Lirung Glacier in the Langtang Valley, Nepal Himalaya, and has shown good performance against stake- and photogrammetry-based cliff melt measurements, though these have been limited to four specific cliffs (Buri and others, 2016a, 2016b). The model has also shown an excellent ability to reproduce weekly melt rates at other monsoonal debris-covered glaciers (Kneib and others, 2022). We did not install stakes on the cliff surface at Trakarding Glacier; therefore, we validated the model performance by comparing the modelled ice cliff morphology with the observed ice cliff morphology from aerial photogrammetry. First, we detected more than 200 ice cliffs (hereafter 'surviving ice cliffs') that remained between the 2018 and 2019 manually digitised inventories (Sato and others, 2021). Then, we randomly selected 100 of these surviving ice cliffs, avoiding merged/split ice cliffs. We compared the cliff map-view area, cliff inclined area (actual slope surface), slope, and aspect of

the modelled cliffs at the end of the modelling period with those of the observed cliffs. The cliffs were categorised as stream- or pond-influenced when located closer than 40 m to either of these features (Kneib and others, 2023), and this validation exercise was conducted for each type of ice cliff.

We also used the same 100 selected cliffs to estimate the sensitivity of the model to its parameters. We ran the cliff backwasting model 22 times, individually increasing/decreasing the five fixed physical and six meteorological parameters (Table S2). We change surface roughness, debris/ice emissivity, and debris/ice albedo as physical parameters. We chose air temperature, incoming short-/long-wave radiation, debris surface temperature, relative humidity, and wind speed as meteorological parameters. These meteorological parameters were obtained at AWS (Figs. 1d and Table 1) and estimated/interpolated on each cliff using temperature lapse rates and correlation between debris and air temperature (Figs. 2 and 3). Owing to our higher spatial resolution (1.0 m instead of 3.0 m) and longer modelling period (year-round rather than five months), we compared the results of sensitivity tests only on upper/lower parameter bounds taken from Buri et al. (2021) to reduce the computational cost. The parameters and ranges used in the one-at-a-time sensitivity test were taken from Buri et al. (2021) using the same dynamic cliff backwasting model. In the previous study, 100 Monte Carlo simulations were run on 40 ice cliffs to estimate the model uncertainty. We also tested the model using a coarser resampled DEM (3.0 m) to assess the effect of resolution.

2.6. Glacier mass balance and mass loss contribution of ice cliffs

To estimate the mass loss contribution of ice cliffs to the glacier-scale mass balance, we employed the surface elevation change provided by Hugonnet and others (2021), as our photogrammetric datasets do not cover the entire glacier. The glacier-wide mass balance on Trakarding Glacier was calculated using a modified GAMDAM glacier inventory (Section 2.1) and the surface elevation change rate during 2015–2019. The uncertainty of this glacier thinning rate has been reported as ± 0.17 m a^{-1} in the target region (Hugonnet and others, 2021). The glacier-averaged surface elevation change rate was converted to glacier mass balance (m w.e. a^{-1}) using the bulk density of ice in debris-covered areas (0.9) relative to the density of water (Miles and others, 2018). We also calculated the mass balance of the debris-free Trambau Glacier to evaluate the contribution of ice cliff mass loss to the mass loss of the whole Trambau–Trakarding glacier system. Then, we used 0.85 as the density of ice (accounting for firn zones) to calculate the glacier-wide mass balance (Huss, 2013). These glacier-wide mass balances indicate net ablation, including accumulation. Hence, we calculated mass loss only in the ablation zone of the debris-covered tongue (Fig. S3) of Trakarding Glacier to evaluate the contribution of ice cliff melt to only debris-covered part. To estimate mass loss on the debris-covered tongue, we calculated the mean emergence velocity (V_e, m a^{-1}) from the upper and lower ice flux as follows (e.g. Nuimura and others, 2011; Miles and others, 2018; Fig. S3):

$$V_e = \frac{(q_{in} - q_{out})}{A},\tag{6}$$

where q_{in} and q_{out} are the ice fluxes at the upper and lower boundaries (m^3 a^{-1}; Fig. S3), respectively, and A is the area of the target zone (m^2). The ice fluxes q (q_{in} and q_{out}, m^3 a^{-1}) were calculated by

$$q = W \cdot h \cdot v \cdot \cdots\tag{7}$$

where W is the width of the ice flux gate (m), h is ice thickness (m), and v is depth-averaged glacier velocity (m a^{-1}). We employed the published ice thickness (h) from Farinotti and others (2019) (Fig. S3). The depth-averaged velocity (V_c) was assumed to be 90% of the surface velocity estimated from photogrammetry-based orthoimages (Sato and others, 2021), following previous studies (e.g. Miles and others, 2018; Sato and others, 2022). We then set simple upper/lower flux gates to cover most of the debris-covered area (Fig. S3). Finally, the mass balance of the debris-covered tongue (*MB*, m w.e.) was calculated as follows:

$$MB = \left(\frac{dh}{dt} - V_e\right) \cdot \frac{\rho_i}{\rho_w},\tag{8}$$

where dh/dt is the mean surface elevation change rate on the debris-covered tongue (m a^{-1}), and ρ_w is the density of water (1000 kg m^{-3}).

Trakarding Glacier is a lake-terminating glacier; therefore, its terminus has retreated and been losing mass through calving and frontal ablation. Almost all previous studies dealing with ice cliff melt effects have focused only on land-terminating debris-covered glaciers (e.g. Brun and others, 2018; Buri and others, 2021; Zhao and others, 2023). To compare our results with these previous studies, we estimated terminus volume loss and eliminated it from the glacier mass balance. Terminus volume loss V_t (m^3) can be theoretically determined from the change in ice front position and ice flux at the terminus (e.g. Wei, 2021), as follows:

$$V_t = V_f + V_r,\tag{9}$$

where V_f and V_r are volume losses (m^3) derived from terminus ice flux and terminus retreat, respectively. Although the lake depth at the terminus is required to calculate V_f and V_r, the elevation change dataset used to calculate the glacier-wide mass balance in this study (Hugonnet and others, 2021) does not account for glacier mass loss below the lake surface. Therefore, only the mass loss above the lake is needed to exclude the calving effect from the glacier mass balance. We calculated ice flux above the lake surface (V_f) at the glacier terminus as follows:

$$V_f = W_t \cdot h_l \cdot v_t,\tag{10}$$

where W_t is the glacier width at the terminus (m), h_l is the ice thickness height above the lake surface (m), and v_t is the depth-averaged velocity at the terminus (m a^{-1}). We used photogrammetry-based DEM and surface velocity data for the study period to compute h_l and v_t (Sato and others, 2021). We also used elevation change above the lake surface of the retreating terminus portion area obtained from photogrammetry-based DEMs to calculate the terminus volume loss (V_r).

Finally, we calculated the enhancement factor (EF) (e.g. Brun and others, 2018; Buri and others, 2021), which measures the relative cliff melt contribution to the relative cliff area for the debris-covered tongue, Trakarding Glacier, and Trambau–Trakarding glacier-system-scale mass loss. The EF is defined as follows:

$$EF = \frac{\frac{V_{cl}}{A_{cl}}}{\frac{V_{gl} - V_{cl}}{A_{gl} - A_{cl}}},\tag{11}$$

where V_{gl} and V_{cl} are the volume losses, and A_{gl} and A_{cl} are the planimetric areas of the glacier surface and ice cliffs, respectively.
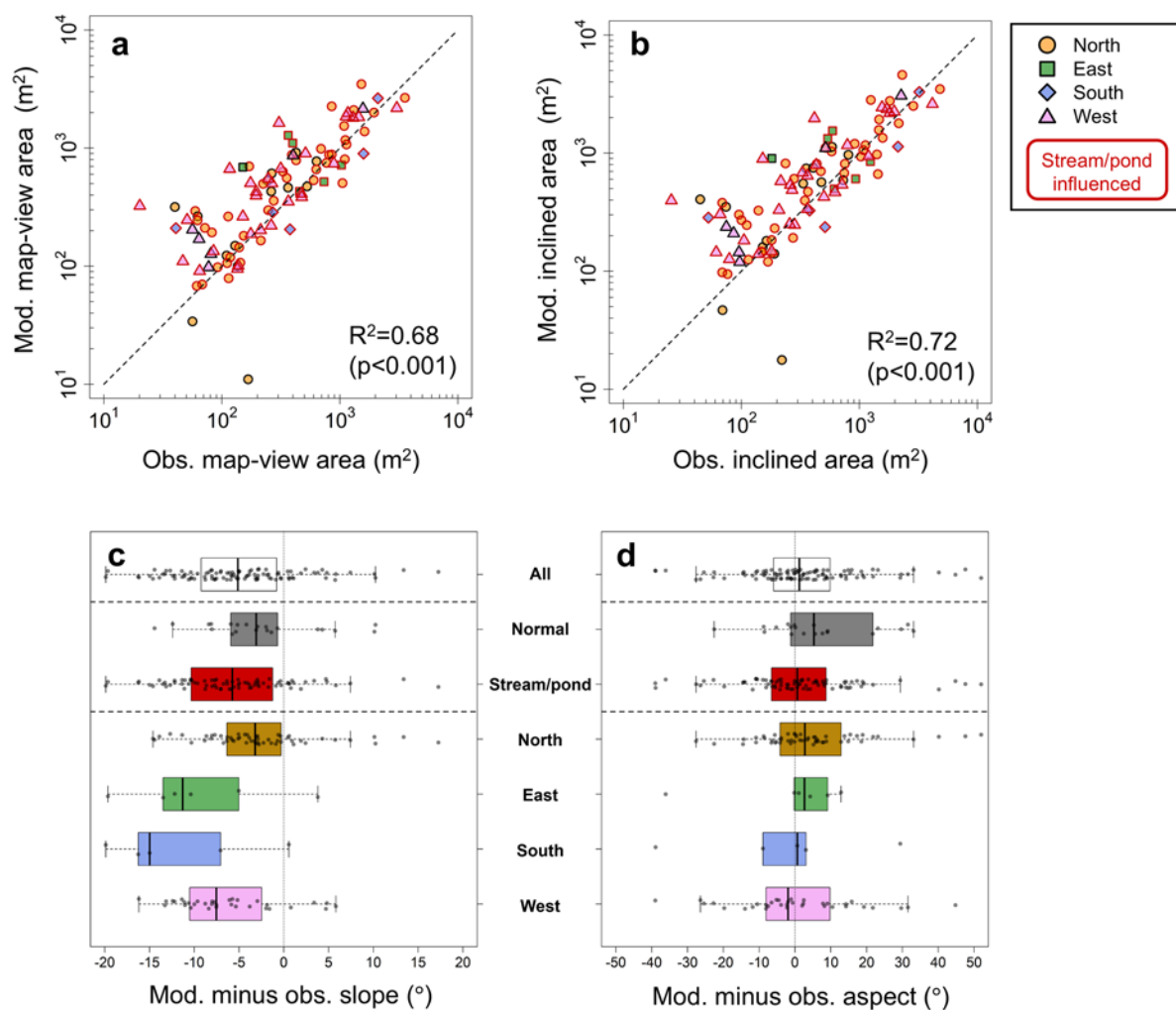
Figure 4. Comparison of observed (obs.) and modelled (mod.) ice cliff shapes for 100 surviving ice cliffs in October 2019, showing map-view area (a), inclined area (b), slope difference (c), and aspect difference (d) of ice cliffs. The red outlines in (a) and (b) indicate stream- or pond-influenced ice cliffs (section 2.5), and plot shapes/colours show original ice cliff aspects in October 2018. The R-squared values in (a) and (b) are from linear regressions between observed and modelled ice cliff map-view/inclined areas. Boxes in (c) and (d) show the 25th–75th percentiles, and black dots depict individual errors on the modelled ice cliff slope and aspect. In (c) and (d), 'stream/pond' ('normal') indicates whether ice cliffs are influenced (or not) by a stream/pond.

3. Results

### 3.1. Model output and sensitivity

We compared modelled and observed ice cliff morphology for the selected 100 surviving ice cliffs used for validation (Fig. 4). The mean residuals in observed ice cliff shape and model output were 165 m^2 for the map-view area and 154 m^2 for the inclined area (Fig. 4a and b), corresponding to 32% of the mean cliff map-view area and 22% of the inclined area, respectively. Considering the mean perimeter length of the ice cliffs (143 m), the mean residual of the map-view area represents a 1.1-pixel overestimate of the outward expansion of the geometry of the cliffs in the dynamic cliff backwasting model. Excessive expansion of the cliff area can lead to overestimation of cliff mass loss; conversely, it can also lead to underestimation of the yearly ice cliff melt rate [Eq. (3)] The model tends to make the cliffs downwasting (surface lowering) more than they would in reality, resulting in shallower slopes after one year (mean residual of −4.5°; Fig. 4c). However, there is no notable difference in the ice cliff aspect (mean residual of 3.0°; Fig. 4d). The errors of these validations were aggregated in

cliff aspect and stream/pond-influenced (or not) type ice cliffs (Fig. 4a–d). However, there were no significant differences between categories.

Examples of modelled ice cliffs extracted from the stagnant part (surface velocity less than 3 m a^{-1}; Figs. 5 and S4) show how cliff geometry changes with each computational step (Fig. 5a and b). The model outputs seem to reconstruct the morphological changes on the ice cliff that have become less steep (Fig. 5b). Furthermore, as the simulation was performed at a high spatial resolution (1.0 m), the spatial heterogeneity of incoming radiation due to the complex morphology and the melt gradient within individual ice cliffs are well represented (Figs. 5c–e and S4).

The model sensitivities were tested on 12 parameters (23 patterns considering upper/lower bounds) for the 100 surviving ice cliffs. We calculated the relative residual in each cliff volume loss for the original parameters and the upper/lower bounds of the tested parameters (Fig. S5a–c). For almost all tests in the chosen range, the median absolute deviation in cliff volume loss did not exceed 15%, except for the incoming longwave radiation and DEM resolution tests (Fig. S5a–c). When the input DEM was resampled to
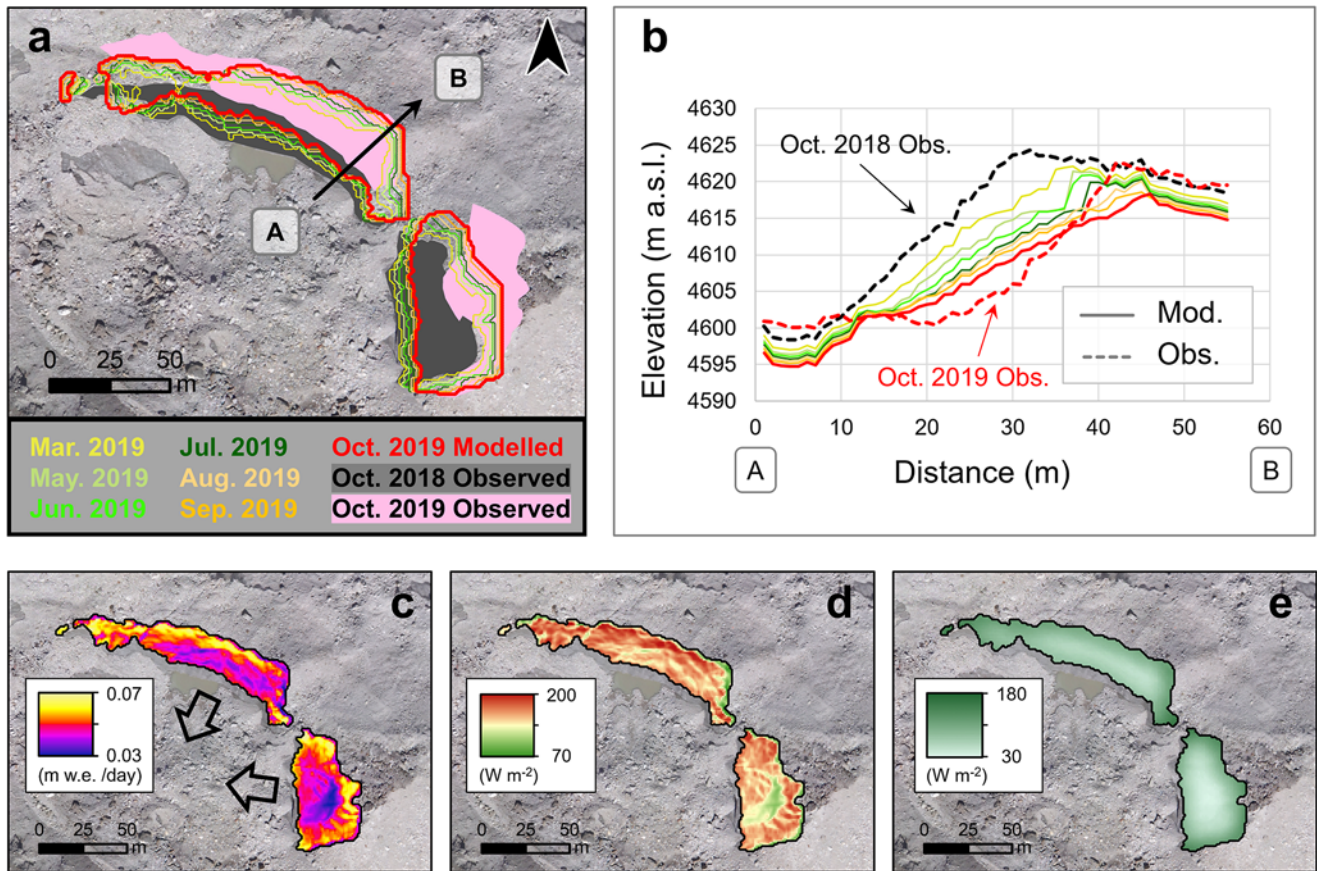
Figure 5. Examples of cliff backwasting model outputs. (a) Outlines of changes in ice cliff geometry and (b) changes in elevation profiles of ice cliff slope, compared with observations. (c–e) Monthly averaged values of (c) melt rate, (d) incoming direct shortwave radiation, and (e) longwave radiation from surrounding debris in May 2019. The black arrow across the cliff in (a) indicates the elevation profile in (b). The colours of the ice cliff outlines and elevation profiles in (a) and (b) depict the respective geometry updates. Pink and grey polygons in (a) are observed ice cliff shapes. Hashed lines in (b) are observed ice cliff elevation profiles from Sato and others (2021). Arrows in (c) indicate aspects of the two example ice cliffs.

3.0 m resolution, the mean residual of relative volume difference was +82%, which is a substantial increase in volume loss (Fig. S5c). This remarkable increase in volume loss is not due to an increase in the melt rate of ice cliffs but rather to unrealistic expansions in cliff size during the simulation period (Fig. S6).
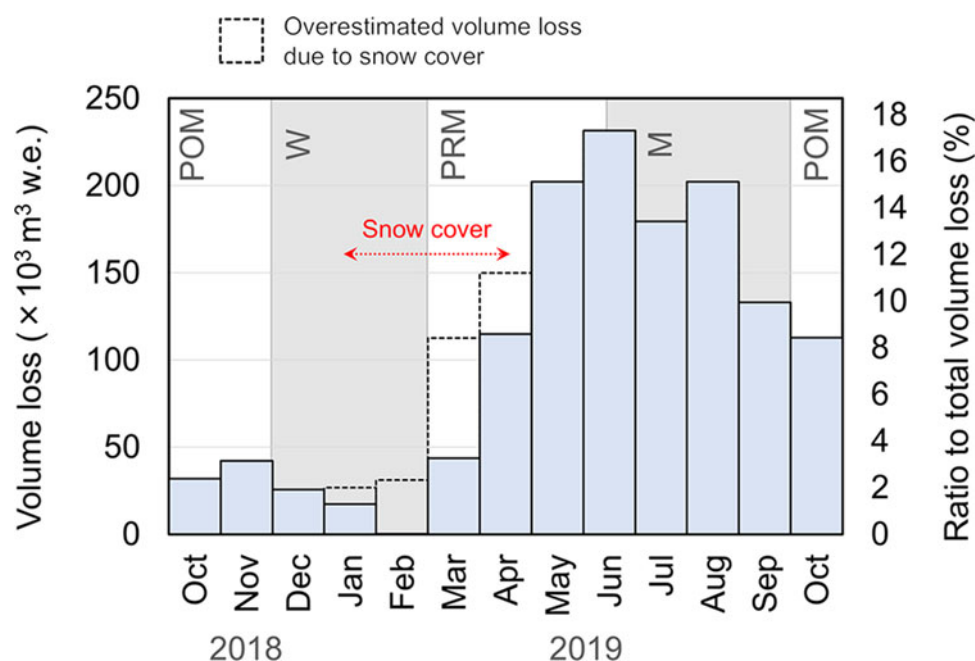
3.2. Volume loss of ice cliffs

We calculated the volume loss of 479 ice cliffs spread over the entirety of Trakarding Glacier with 1 hour time steps. The total volume loss of the ice cliffs during one year (18 October 2018 to 18 October 2019) was 1.34×10^6 m³ w.e. The monthly ice cliff volume losses of the entire glacier are summarised in Fig. 6. The largest volume loss was observed in June (2.32×10^5 m³ w.e., 17% of the annual volume loss). The monthly volume loss of ice cliffs increased after March, at the end of the winter season. Monthly cliff volume losses from May to August (summer monsoon season) each exceeded 12% of the annual volume loss. We were able to clearly confirm snow cover in time-lapse images between January and April (Fig. 6). Most of the days in February and March were snow-covered, which reduced the annual volume loss of ice cliffs by 10% compared with the case where snow cover was ignored (i.e. potential volume loss). Our simulation of the whole-year range showed that 18% of the annual mass loss occurred outside of the ablation season (November to April; Fig. 6).

We divided the ice cliff volume loss into eight aspect bins (Figs. 7a and S7a). The largest volume loss was observed in the north-facing cliff group (337.5°–22.5°), with 2.88×10^4 m³ w.e. (21% of the total volume loss). The north-, northeast-, and northwest-facing cliff groups account for >50% of the total volume loss of all ice cliffs on Trakarding Glacier. However, it should be noted that the area of ice cliffs was not uniform across aspect bins, and north-facing ice cliffs predominated (Fig. 7b).
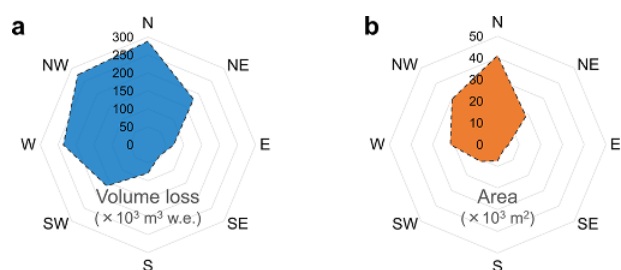
3.3. Ice cliff melt rate

Cliff melt rate was calculated using monthly/annual time steps for each ice cliff. The mean and median melt rate of all ice cliffs on Trakarding Glacier were 2.7×10^{-2} and 2.6×10^{-2} m w.e. d⁻¹, respectively. The ice cliff melt rate varied, ranging from 1.1×10^{-2} to 7.3×10^{-2} m w.e. d⁻¹ for the 479 ice cliffs. We estimated the relationship between ice cliff melt rate and cliff aspect/elevation (Fig. 8a and b). Then, we applied harmonic and linear regression to each parameter and found that both parameters had a significant relationship with ice cliff melt rate ($p < 0.001$). However, ice cliff aspect better explained the melt rate ($R^2 = 0.48$; Fig. 8a) than did cliff elevation ($R^2 = 0.03$; Fig. 8b). In this harmonic regression between the aspect and melt rate of the ice cliffs, the maximum melt rate occurred for south-facing cliffs (3.9×10^{-2} m w.e. d⁻¹ at 181°), 1.8 times higher than the minimum value

Figure 6. Monthly ice cliff volume loss and its ratio to total cliff volume loss. The unfilled dashed bars from January to April represent overestimated ice cliff volume loss without considering snow cover. The October 2018 period is from the 18th to the 30th (12 days), and the October 2019 period is from the 1st to the 18th (18 days). The POM, W, PRM, and m indicate post-monsoon, winter, pre-monsoon, and monsoon season (grey shaded areas depict winter and monsoon season).

Figure 7. Aspect distribution of (a) ice cliff volume loss from October 2018 to October 2019 and (b) ice cliff map-view area.

for north-facing cliffs (2.1×10^{-2} m w.e. d^{-1} at 1°; Figs. 8a and S7b).

We also calculated monthly ice cliff melt rates and aggregated them with respect to these aspects (Fig. 9 and Table S3). The results showed clear seasonality in ice cliff melt rate: the highest melt rate was observed in June (median of 6.5×10^{-2} m w.e. d^{-1}), and the lowest in December (3.4×10^{-3} m w.e. d^{-1}), with an estimated difference of almost 20-fold between them. The ice cliff melt rate continued to decrease from the start of the simulation until December, recording its minimum value. From January approaching the ablation season, the melt rate increased, reaching its peak in June (Fig. 9).

Notably, we detected a relationship between aspect and the seasonal dependence of ice cliff melt rate. During the cold season (October 2018 to February 2019), melt rates show a strong aspect dependence, with the melt rate decreasing in order from south- to west- to east- to north-facing cliffs (Fig. 9). However, the difference in ice cliff melt rate between cliffs with different aspects decreased approaching the melt season. From June to August 2019, there was no significant difference in melt rate between north- and south-facing cliffs (via Student's t-test; $p > 0.05$). In June,

when the maximum melt rate was observed, the melt rate was almost equal for all ice cliff aspects (Fig. 9). Focusing on the contrasting south- and north-facing ice cliffs, the strongest aspect dependence of melt rate (relative difference) was in December, when the median value of the melt rate of south-facing ice cliffs (1.9×10^{-2} m w.e. d^{-1}) was more than 20 times higher than that of north-facing ice cliffs (8.5×10^{-4} m w.e. d^{-1}). In absolute terms, the difference between the melt rates of the south- and north-facing ice cliffs reached its maximum at the end of October 2018, when the melt rate of south-facing ice cliffs (3.6×10^{-2} m w.e. d^{-1}) was 2.7×10^{-2} m w.e. d^{-1} higher than that of north-facing ice cliffs (9.0×10^{-3} m w.e. d^{-1}). It should be noted that this period (October 2018) does not cover the whole month (Table S3).

3.4. Energy balance

We aggregated the component of the energy balance that leads to ice cliff ablation each month (Fig. 10a and Table S4). Fig. 10a shows the daily mean energy balance for each month. It should be noted that almost allmelt of ice cliffs occurred in daytime (between 08:00 and 17:00). In addition, during the timesteps when the energy balance became negative, Q_m was treated as zero (no melt; Steiner and others, 2015). In terms of the contribution to ice cliff melt, incoming shortwave radiation (I_{in}) was the most significant component in the energy balance, which consists of direct shortwave radiation (I_s) and diffuse shortwave radiation from the sky (D_s) and terrain (D_t) (Fig. 10a). The annual mean of I_n is 163 W m^{-2}, which explains 63% of the melt component (positive energy flux for melt). I_{in} shows seasonal variation between ~ 100 and 250 W m^{-2}, and the highest I_{in} was observed in May (249 W m^{-2}). There was also seasonal variability in the ratio of I_{in} components (Fig. 10d). The annual mean energy fluxes of I_s and D_s were 63 and 11 W m^{-2} (55% and 39% of I_{in}), respectively (Table S4). I_s was generally
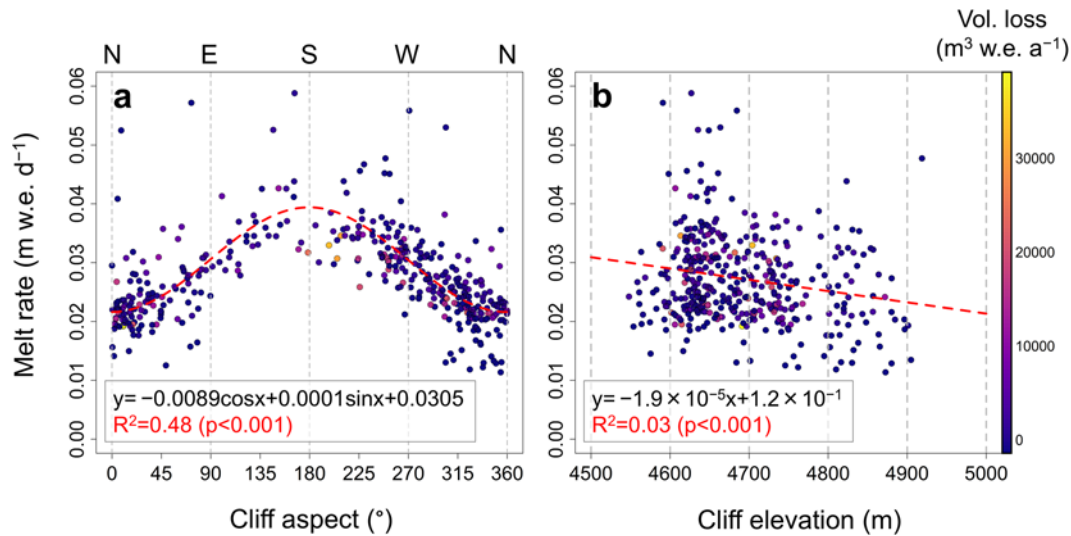
Figure 8. Individual ice cliff melt rates over the simulation period as a function of (a) cliff aspect and (b) cliff elevation. dashed red lines in (a) and (b) are harmonic/linear fittings of ice cliff melt rate. The colour scale indicates the volume loss at individual ice cliffs from October 2018 to October 2019.
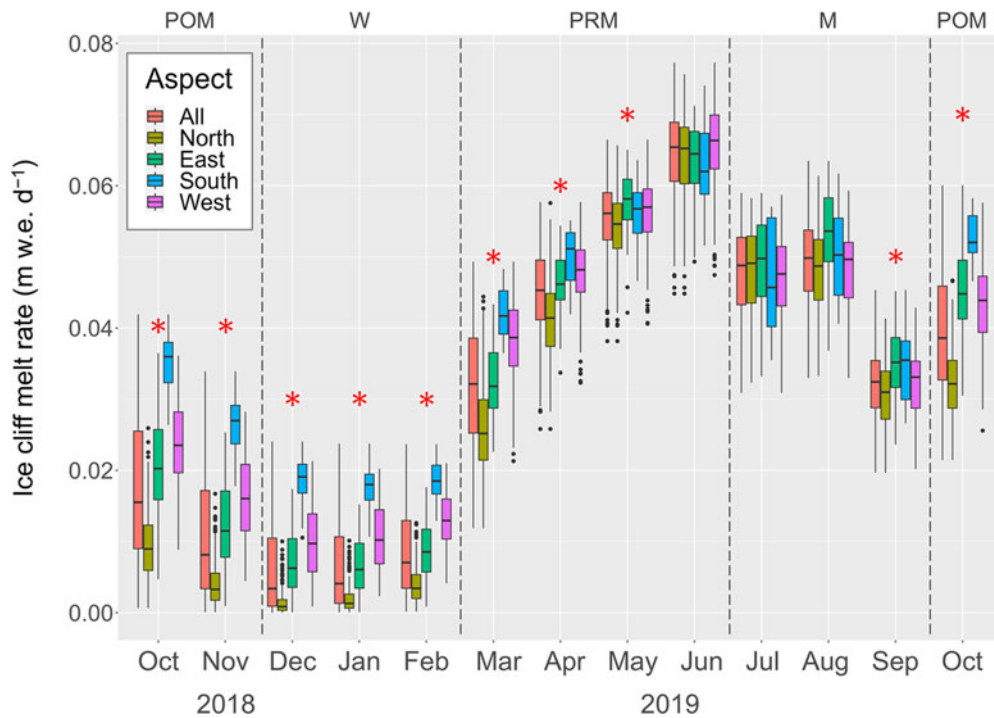

Figure 9. Monthly ice cliff melt rate plotted over time with respect to ice cliff aspect. Coloured boxes show the 25th–75th percentiles, and black dots represent outliers. Red asterisks indicate a significant difference in melt rate between north- and south-facing ice cliffs in each month ($p < 0.05$; student's t-test).

more predominant than D_s, although D_s became larger in July and September, accounting for more than 50% of the total incoming shortwave radiation (Fig. 10d). D_t was the minor component and remained below 10% relative to I_{in} throughout the target period (Fig. 10d).

We compared the monthly Q_m with monthly air temperature and shortwave radiation observed at the AWS (Fig. 10g and Table S5). A significant correlation was found between Q_m and daytime shortwave radiation ($r = 0.97$, $p < 0.001$) but not between Q_m and air temperature at the AWS. For incoming longwave radiation (L_{in}),

the mean of longwave radiation fluxes from the sky (L_s) and debris (L_D) were 135 and 102 W m^{-2} (57% and 43% of L_{in}) during the target period, respectively (Table S4). In this study, debris surface temperature was forced by air temperature (Section 2.3; Fig. 3); even considering the topography (debris view angle) for individual ice cliffs, there was a significant correlation between monthly AWS air temperature and L_d ($r = 0.77$, $p < 0.05$). Mean net longwave radiation (L_n) was constantly negative throughout the year, which indicates a consistent negative influence on cliff ablation at Trakarding Glacier (Fig. 10a). Sensible and latent heat fluxes
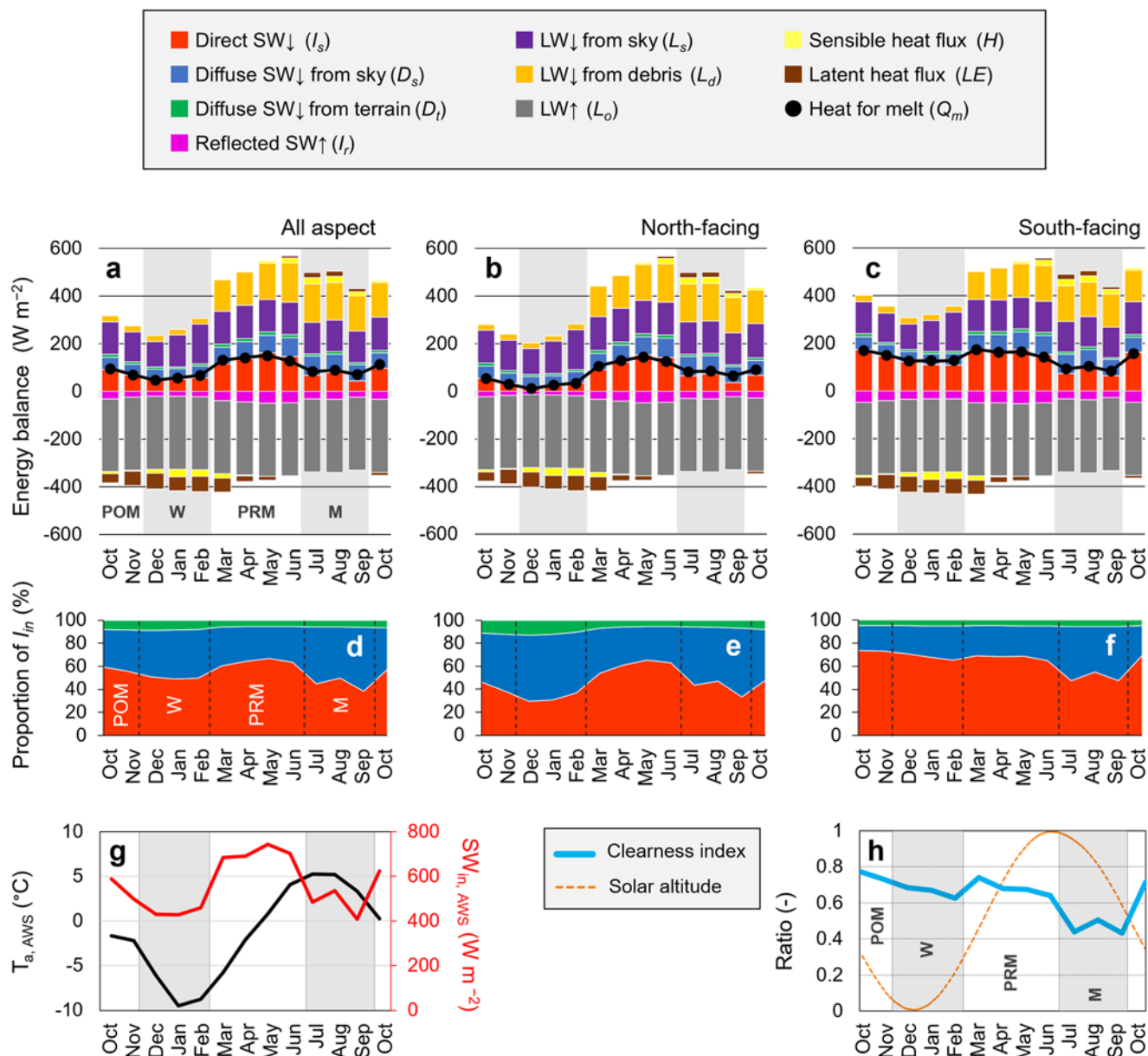
Figure 10. Mean energy balance of all (a), north-facing (b), and south-facing (c) ice cliffs. Components of incoming shortwave radiation (i_s, d_s, and d_t) of all (d), north-facing (e), and south-facing (f) ice cliffs. (g) Observed air temperature ($t_{a,\text{AWS}}$) and incoming shortwave radiation ($sw_{in,\text{AWS}}$) at the AWS. (h) Clearness index at the AWS (section 2.4) and normalised solar altitude for Trakarding Glacier. Note that almost of the melt of ice cliffs were occurred in daytime. During the time steps when the energy balance became negative, the heat for ice cliff melt (q_m) was treated as zero.

Table 2. Summary of area, mass loss, and enhancement factor (EF) of ice cliffs on the debris-covered tongue, Trakarding glacier, and the Trambau–Trakarding glacier system. The terms 'incl.' ('excl.') v_t indicate that the terminus volume loss is contained (not contained) in glacier mass loss. Glacier mass losses was calculated from the surface elevation change dataset of Hugonnet and others (2021). The target regions of the debris-covered tongue, Trakarding glacier, and the Trambau–Trakarding glacier system are shown in figures 1a and S3. Note that the mass loss of ice cliffs on snow-covered days was excluded from all results

|		Debris-covered tongue	Trakarding glacier	Trambau–Trakarding glacier system
Glacier area (km^2)		2.71	8.21	31.54
Ice cliff area (km^2)			1.38×10^{-1}	
Relative ice cliff area (%)		5.1	1.7	0.4
Averaged mass balance (m w.e. a^{-1})		−1.48	−0.77	−0.58
Cliff mass loss (km^3 w.e.)			1.34×10^{-3}	
Glacier mass loss (km^3 w.e.)	Incl. V_t	5.21×10^{-3}	6.35×10^{-3}	1.82×10^{-2}
	Excl. V_t	4.04×10^{-3}	5.17×10^{-3}	1.71×10^{-2}
Cliff melt contribution (%)	Incl. V_t	25.6	21.0	7.3
	Excl. V_t	33.1	25.8	7.8
EF	Incl. V_t	6.4	15.6	18.0
	Excl. V_t	9.1	20.3	19.3

either inhibited or promoted cliff melt depending on the season but did not exceed 10% of the positive/negative energy fluxes in most months (Fig. 10a).

The energy balance shows contrasting patterns depending on aspect, especially between north- and south-facing ice cliff groups. The energy balance components for the north-/south-facing cliff aspects are summarised in Fig. 10b and c. The annual averages for north- and south-facing Q_m were 76 and 138 W m^{-2}, respectively (Table S4). The average Q_m for south-facing ice cliffs is 1.8 times higher than that for north-facing ice cliffs. This result supports the harmonic regression of the annual melt rate estimated from all ice cliffs (Fig. 8a). I_s values of north- and south-facing ice cliffs are notably different, with the annual mean of I_s of south-facing ice cliffs (133 W m^{-2}) being $\sim$ 2 times higher than that of north-facing ice cliffs (Fig. 10b–c and Table S4). This difference in I_s contributes to the contrasting Q_m between north- and south-facing ice cliffs. The mean annual ratios of I_s and D_s for north-facing cliffs were 49% and 44%, and those for south-facing cliffs were 65% and 30%, respectively (Table S4). The aspect dependence of the I_{in} component amplified/decreased according to season, being more pronounced in the cold season (Fig. 10e and f). The average I_s from December to February, defined as the winter season in this study, was 26 W m^{-2} for north-facing ice cliffs and 115 W m^{-2} for south-facing ice cliffs. During the winter season, the I_s of north-facing cliffs accounted for less than 35% of I_n, whereas south-facing cliffs accounted for $\sim$ 70% (Fig. 10e and f). However, the difference in shortwave radiation flux components decreased towards the monsoon season, with I_s accounting for $\sim$ 50% of I_{in} for both north- and south-facing ice cliffs (Fig. 10e and f).

3.5. Mass loss contribution and melt enhancement of ice cliffs

We estimated the glacier mass balance and compared it with the mass loss of ice cliffs (Table 2). It is noted that these results consider the effect of snow cover, which reduced ice cliff mass loss in the cold season (Section 3.2). The glacier-wide mass balance of Trakarding Glacier in 2015–2019 was -0.86 ± 0.15 m w.e. a^{-1}. Comparing the glacier-scale and ice cliff mass losses, ice cliffs accounted for 23.2% of the total glacier mass loss, despite covering only 1.7 % of the glacier surface. When the terminus mass loss (V_t) was excluded from the total glacier mass loss, the total ice cliff mass loss accounted for 25.8% of the glacier-scale mass loss (Table 2). The EF [Eq. (11)] of the ice cliffs relative to Trakarding Glacier was 15.6 (including V_t) and 20.3 (excluding V_t). With respect to the mass loss of the debris-covered tongue (ablation zone), ice cliffs covered 5.1% of the surface area and contributed 33.1% of the glacier-scale mass loss (excluding V_t; Table 2). The EF of ice cliff melt was 9.1 on the debris-covered tongue. We also compared our modelled ice cliff ablation with mass loss measured at seven stakes in the debris-covered area (Figs. 1d and 11). The mean annual mass balance at stakes was -1.2 m w.e. (ranging from -2.2 to -0.6 m w.e.), and the mean debris thickness at the stake points was 15 cm (12–65 cm) (Fig. 11). The mean annual melt rate of the ice cliffs (-9.9 m w.e.) was 8.3 times higher than the average measured for debris-covered ice. From these results, the ice cliff EF on the debris-covered tongue that was estimated from remote-sensing data (9.1) is considered reasonable compared with the observed EF (8.3).

We also estimated the contribution of ice cliff mass loss to that of the Trambau–Trakarding glacier system (Table 2). The ice cliffs had an area relative to the glacier system of 0.4% and accounted for 7.3% (including V_t) and 7.8% (excluding V_t) of the total glacier
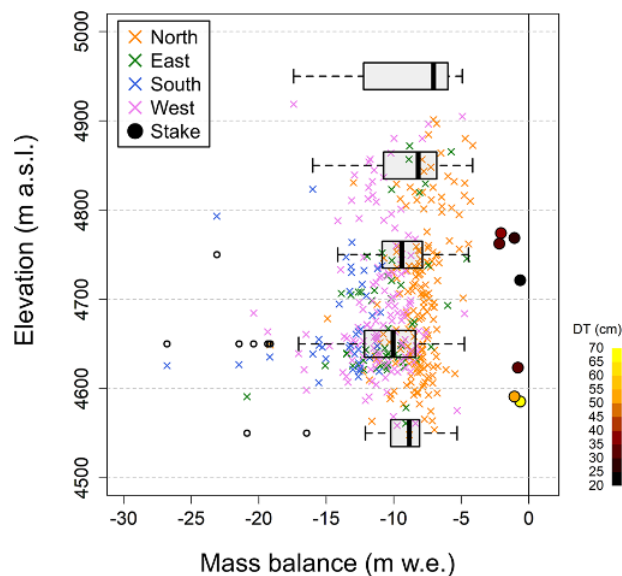
Figure 11. Annual ablation of ice cliffs (coloured crosses) and mass balance at stakes (coloured circles) from October 2018 to October 2019. The box plots are ice cliff ablation rates summarised for 100 m elevation bins. Cross colours indicate ice cliff aspect, and circle colours denote debris thickness (DT; cm) measured at stakes. Grey boxes show the 25–75th percentiles, and unfilled dots represent outliers.

system mass loss. In addition, the cliff EF in the glacier system was 18.0 (including V_t) and 19.3 (excluding V_t) (Table 2). The cliff EF for the Trambau–Trakarding glacier system was smaller than that of only Trakarding Glacier when calving volume loss was excluded (Table 2).

4. Discussion

Previous studies have estimated ice cliff melt using energy balance approaches (e.g. Sakai and others, 2002; Han and others, 2010; Buri and others, 2021) for the main ablation season (May to October). However, our simulation is the first to estimate full-year and glacier-scale ice cliff melt. Our simulation also considers cliff geometry updates, which is the only effective method for estimating long-term ice cliff melt by reconstructing realistic cliff fluctuations (Buri and others, 2016b). Our study is the first attempt to apply such a dynamic model to another site that has different conditions from the Langtang region. Furthermore, this study is the first to use high-resolution (1.0 m) terrain data to reconstruct the morphology of ice cliffs as input with validated its geomorphological change with as many as a hundred ice cliffs. Here, we discuss the implementation of our modelling approach, the role of ice cliffs as melt hotspots on Trakarding Glacier, and the seasonal melt characteristics of ice cliffs.

4.1. Performance of the dynamic cliff backwasting model

We validated the cliff shape of the modelled output and showed that of all metrics (size, slope, and aspect; Fig. 4a–d). We showed that the cliff area was slightly overestimated by the dynamic model (1.1-pixel overestimate of the outward expansion; Sect. 3.1). As the morphology of the ice cliffs was updated in a non-linear manner every month, it is difficult to quantify the volume loss uncertainty

associated with the overestimation of the ice cliff area expansion at the final output. Here, we assume that the overestimation of ice cliff area expansion occurred linearly during the simulation period, which means that the overestimation of ice cliff area changes could cause up to a 16% overestimation of cliff volume loss. Furthermore, cliff slope was underestimated by the model (Fig. 4c). The lack of representation in the model of physical collapse and thermal undercutting caused by channels and ponds might have contributed to this change in ice cliff morphology beyond that expected from the energy balance. Such changes in ice cliff morphology have been observed on other debris-covered glaciers (e.g. Kraaijenbrink and others, 2016; Kneib and others, 2022; Petersen and others, 2024). The median residuals of slope angle between stream/pond-influenced and normal (not stream/pond-influenced) ice cliffs were −5.7° and −3.1°, respectively (Fig. 4c), indicating no significant difference. However, this lack of difference may be due to the limited sample size (only 21 normal ice cliffs) and to the difficulty of assessing the strength of the link between hydrology and cliff evolution from remote-sensing data only (Kneib and others, 2023). Petersen et al. (2024) reported that stream-influenced ice cliffs have incisions formed by supraglacial channels in their underpart and steeper slopes than those of ice cliffs that are not stream influenced at Kenicott Glacier, Alaska. This stream effect also leads to the generation of wider angles between cliff slopes and backwasting ramps (the opposite side mound of the cliff surface). Although the dynamic cliff backwasting model used in this study does not take into account such an effect of supraglacial channels, this effect should be incorporated into future dynamic models to estimate more realistic ice cliff fluctuations.

We tested the sensitivity of the model to 12 physical and meteorological parameters (22 patterns) for the 100 ice cliffs used for validation (Fig. S5a and b). The uncertainty in our simulation does not appear to differ from that of previous work: the sensitivity analysis shows a similar response to parameters as reported by Buri et al. (2021), using the same dynamic cliff backwasting model. Buri et al. (2021) reported an uncertainty of 3355 m^3 w.e. per cliff in the cliff backwasting model for the Langtang region based on 100 Monte Carlo simulations. In the work of Buri et al. (2021) in the Langtang region, the source ice cliff inventory was delineated from SPOT-6 satellite imagery (1.5 m resolution; Steiner and others, 2019), and those authors reported that the median extracted ice cliff size was 845 m^2, seven times larger than the median ice cliff size of Trakarding Glacier (112 m^2). Application of the uncertainty in volume loss of ice cliffs estimated by Buri et al. (2021) to the median cliff size of Trakarding Glacier yields an uncertainty of volume loss per cliff of 445 m^3 w.e in this study. Multiplication of the uncertainty per ice cliff by 479 ice cliffs yields a value of 16% of the total volume loss of all ice cliffs on Trakarding Glacier (2.21×10^{-4} km^3 w.e.).

We also tested the effect of the resolution of the input DEM, and this simulation showed a remarkable increase in mass loss compared with the baseline setting due to cliff expansion (Fig. S5c). The resolution of the DEM is one parameter that significantly influences the estimated expansion of ice cliffs (Fig. S6). If coarse satellite-based DEMs (2–3 m) are used in this dynamic model, the parameters suppressing the expansion/shrinkage of ice cliffs should be optimised for each case. In particular, two parameters should be considered: the slope threshold, which controls cliff reburial, and the negative buffer size, which controls the shrinkage and expansion of cliffs (Buri and Pellicciotti, 2018).

4.2. Ice cliffs as melt hot spots of Trakarding Glacier and the Trambau–Trakarding glacier system

Our study indicates that ice cliffs were responsible for a substantial portion of mass loss at Trakarding Glacier (Table 2). Although ice cliffs covered only 1.7% of the surface of Trakarding Glacier, they contributed 25.8% of the glacier-scale mass loss when the terminus mass loss was considered. Buri et al. (2021) used the same energy balance model and estimated the contribution of ice cliffs to glacier-scale mass loss for four glaciers in Langtang Valley. Those authors reported that the contribution of cliffs to glacier-scale mass loss ranged from 7% (Shalbachum Glacier) to 17% (Langtang Glacier). Our simulation used a higher-resolution original orthoimage/DEM (0.2 m/0.2 m spatial resolutions; Sato and others, 2021) compared with the Langtang study (1.5 m/3.0 m; Steiner and others, 2019) to generate the ice cliff inventory. Hence, more small cliffs were extracted at Trakarding on account of the difference in resolution of images for extracting ice cliffs (Kneib and others, 2020; Section 4.1). In addition, we targeted a longer period (1 year) than that of Buri et al. (2021), who computed the melt only for the ablation season. The greater contribution of ice cliff mass loss to glacier-scale mass loss at Trakarding Glacier relative to the Langtang Valley glaciers can be attributed to the following reasons. Trakarding Glacier has a higher density of ice cliffs compared with the glaciers in Langtang Valley (Steiner and others, 2019; Sato and others, 2021; Kneib and others, 2023). In addition, the mass loss in the debris-covered area might be effectively compensated by avalanche accumulation from the headwall, suppressing the mass loss on the glacier surface (Fig. S8). The upper part of Trakarding Glacier, which has progressively separated from the clean Trambau Glacier during the past few decades, has no widespread transition zone from the debris to clean areas (Fig. S8), where melting should be enhanced (e.g. Fyffe and others, 2014; Fyffe and others, 2020). These glacier characteristics appear to have resulted in a higher melt contribution of ice cliffs to glacier-scale mass loss at Trakarding Glacier than at other debris-covered glaciers. Quantifying avalanche accumulation and tracking terminus mass loss will be essential aspects of future work to understand the glacier regime.

Considering the entire Trambau–Trakarding glacier system, ice cliffs accounted for 0.4% of the total area and contributed 7.3% of the glacier-scale mass loss (Table 2, including V_t). Although Trambau Glacier has debris-covered medial moraines and contains some ice cliffs (Kneib and others, 2023), these were not covered by our photogrammetric survey. If these ice cliffs were included, then the ice cliff mass loss and their contribution to the mass loss of the glacier system should be increased. The EF of ice cliffs for the glacier system was 18.0, which is similar to that for Trakarding Glacier (20.3). In general, the EF of ice cliffs is greatly increased when upper clean ice areas are considered, as accumulation by solid precipitation suppresses the glacier mass loss (Buri and others, 2021). In contrast, decreased EF values occur in the case of extended ablation zones. In our target region, the EF of Trakarding Glacier changed little when including the accumulation zone of Trambau Glacier (Table 2). Sunako et al. (2019) reported that the equilibrium line altitude of the Trambau–Trakarding glacier system is ~5800 m a.s.l. and that most of the clean ice part is in the ablation zone. In addition, the mass balance of the lower part of Trambau Glacier (the clean part) is more negative (approximately −5 to −4 m w.e. a^{-1}) than that of Trakarding Glacier (Sunako and others, 2019). As Trambau Glacier (the clean part) has a large ablation zone, the EF of the entire glacier system might therefore show

a similar value to the EF of Trakarding Glacier despite including an accumulation zone (Table 2). Nevertheless, the mass loss of ice cliffs relative to that of the entire glacier system (>7%) can be considered significant in terms of total mass balance or discharge.

4.3. Aspect characteristics of ice cliff melting

Previous studies have addressed the aspect characteristics of cliff melt and reported higher ablation rates on south- to southeast-facing ice cliffs using energy balance approaches (Sakai and others, 1998; Buri and Pellicciotti, 2018). Compared with these experimental studies, our study estimated ice cliff melting rates in a more realistic setting, in which we confirmed a clear dependence of ice cliff melt rate on aspect (Figs. 8a, 11 and S7b). We estimated a harmonic regression between ice cliff aspect and annual melting rate, with the maximum value for south-facing ice cliffs, which was almost twice as high as the lowest value (for north-facing ice cliffs; Fig. 8a). This aspect dependence is ascribed to the difference in incoming direct shortwave radiation between south- and north-facing ice cliffs (Fig. 10b, c, e, and f and Table S4; Section 3.4).

Despite south-facing ice cliffs having higher melt rate, the south-facing ice cliffs accounted for only about 20% of the total volume loss, more than 50% of melt occurred in the population of north-facing ice cliffs (Figs. 7a, S7a, and S7b). This volume loss pattern is attributed to the persistence of north-facing ice cliffs, resulting in their larger proportion relative to other aspects ice cliffs on Trakarding Glacier (Fig. 7b). Previous studies have shown that cliff lifespan is strongly related to cliff aspect. South-facing ice cliffs receive intense shortwave radiation on their cliff top, leading to a gentler slope, so they tend to be buried by debris (Sakai and others, 1998, 2002; Buri and Pellicciotti, 2018). Such a characteristic of incoming shortwave radiation and melt pattern was also confirmed in our simulations (Fig. 5c and d). Conversely, north-facing ice cliffs provide shade on their own surface, thereby extending their lifespan (Sakai and others, 2002). The predominance of north-facing ice cliffs has been confirmed on Trakarding Glacier (Fig. 7b; Sato and others, 2021) and has also been observed in other Himalayan regions (e.g. Watson and others, 2017b; Kneib and others, 2023). Therefore, south-facing ice cliffs, despite having a much higher melt rate than that of north-facing cliffs, are in the minority and do not exceed the total mass loss of north-facing ice cliffs.

4.4. Seasonal fluctuations in ice cliff melt

Our full-year simulation of 479 cliffs provided seasonal fluctuations and aspect characteristics of ice cliff melt. The monthly ice cliff melt rate was not correlated with air temperature but with shortwave radiation observed at the AWS, and the highest melt rate and total volume loss occurred during the pre-monsoon season (Figs. 6, 9, and 10).

In addition, the aspect dependence of ice cliff melt rates was magnified during the winter season but dissipated towards the monsoon season (Fig. 9). These characteristics are ascribed to regime changes in direct shortwave radiation, which accounts for the majority of the energy flux of cliff melt (Fig. 10a; Section 3.4). In the Himalayan region, the solar elevation angle lowers in winter (i.e. the solar zenith angle increases; Cooper, 1969; Fig. 10h). This leads to a strong contrast in the energy balance of ice cliffs, with substantially more direct shortwave radiation being received on south-facing cliffs than on north-facing ice cliffs (Fig. 10b,

c, e, f, and h; Section 3.4). This contrast of incoming shortwave radiation leads to a pronounced difference in winter melt rate between north- and south-facing ice cliffs (Fig. 9). Conversely, the solar elevation angle becomes higher from the end of the pre-monsoon to the monsoon season, which provides more direct shortwave radiation to a broader range of ice cliff aspects (Fig. 10e, f, and h). In addition, during the monsoon season, diffuse short-wave radiation is predominant due to cloud cover shelter in the Himalaya (Fig. 10a; Section 3.4; e.g. Sakai and others, 2002). Thus, the aspect dependence of ice cliff melt rate is expected to disappear during the monsoon season, and the melt rate decreased despite higher temperatures than during the pre-monsoon (Figs. 9 and 10g). This study, therefore, revealed the aspect dependence of ice cliff melt rate (i.e. dependence on direct shortwave radiation) and confirmed that south-facing ice cliffs maintain a high melt rate despite the cold season (Figs. 8a, 9, and 10b–c). Such cliff melts in the cold season should thus be considered in estimating debris-covered glacier melt for glaciers with abundant cliffs at their surface.

4.5. Limitations and future work

This study did not consider ice cliffs that were newly formed during the simulation period. At Trakarding Glacier, almost half of all ice cliffs (235 cliffs; 2.4×10^{-2} km^2) were replaced between 2018 and 2019 (Sato and others, 2021). The mean individual area and total area of these newly formed ice cliffs were relatively small compared with surviving ice cliffs. However, the newly formed ice cliffs exhibited a wide variety of cliff aspects, and the proportion of south-facing newly formed cliffs was higher than that of surviving ice cliffs. We estimated the melt of newly formed cliffs by applying the empirical relationship derived between ice cliff melt rate and aspect to the inventory of newly formed ice cliffs detected by Sato and others (2021) (Fig. 8a). The newly formed ice cliffs had a slightly higher mean melt rate (2.8×10^{-2} m w.e. d^{-1}) than that ice cliffs used in simulation (2.7×10^{-2} m w.e. d^{-1}). When considering mass loss of newly formed ice cliffs, the monthly mass loss of the total ice cliffs increased by 16%. It is impossible to determine when the ice cliffs formed during the one-year simulation period. If we hypothesised that cliffs were formed in the middle of the simulation period (i.e. the annual mass loss of newly formed ice cliffs was reduced by half), then newly formed ice cliffs accounted for only 2% of glacier-scale mass loss. Although it is worth considering the presence of newly formed ice cliffs to estimate the actual contribution of ice cliffs to debris-covered glaciers, this may not be particularly significant on Trakarding Glacier.

Although trials were conducted involving changing model parameters, it was challenging to reconstruct disappeared ice cliffs (i.e. those buried by debris during the simulation period) completely. We compared simulated and observed ice cliffs (Sato and others, 2021), focusing on cliff disappearance (Table S6). Although the model usually represents surviving cliffs well, only 25% of cliffs that should have disappeared at October 2019, disappeared during the simulation period. To estimate ice cliff persistence, not only energy balance should be considered but also changes in surface albedo (e.g. Kneib and others, 2022), cliff calving (e.g. Miles and others, 2017; Watson and others, 2017a), debris mobility (e.g. Westoby and others, 2020), and maintenance effects from adjacent supraglacial ponds/channels (e.g. Anderson and others, 2021b; Kneib and others, 2023; Petersen and others, 2024). Although these processes are difficult to represent, future models of cliff evolution should attempt to incorporate them. The temperature distribution

of the debris surface, which controls incoming longwave radiation, may also influence cliff persistence (Sakai and others, 2002). Previous studies have reported that debris surface temperature is controlled by incoming shortwave radiation and surface aspect (e.g. Kraaijenbrink and others, 2018). In this study, we estimated debris surface temperature from the empirical relationship with air temperature. However, further geometric factors with respect to debris-covered surfaces should be considered when estimating surface temperature for the dynamic model. In terms of glacier scale cliff dynamics, one previous study has developed an ice cliff tracking method to detect their dynamics automatically (Kneib and others, 2021). Such work has the potential to be further automated, possibly with machine learning approaches, which may allow model development to also predict ice cliff dynamics.

This study assumed that all ice cliff melting ceased for entire days when snow cover was observed from time-lapse images (Fig. S2). These time-lapse images covered only the terminus portion of Trakarding Glacier, and the distance of time-lapse camera from the debris-covered surface limited the information that could be obtained from the images. Therefore, the effect of snow cover on individual ice cliffs could not be considered. Girona-Mata et al. (2019) estimated snow line altitude fluctuation at Langtang catchment and reported that snow cover on south-facing slopes melts/retreats more efficiently than that of north-facing slopes owing to incoming shortwave radiation flux, especially in winter. If such mechanisms were applicable to the microtopography of debris-covered glaciers (ice cliff surfaces), then snow cover on north-facing ice cliffs may persist longer than that on south-facing ice cliffs, inhibiting ice cliff melt. This would lead to the aspect dependence of cliff melt rate in cold seasons becoming even more pronounced.

While our simulation did not consider the refreezing of cliff melt water, the incoming energy flux sometimes became negative in the cold season and/or night time. Some previous studies suggested the importance of taking into account refreezing at cliff surfaces (Steiner and others, 2015). Following the Steiner et al. (2015) approach, we estimated the energy available for refreezing at the cliff surfaces. Using the aggregated hourly energy balance for each month (Fig. S9), we first detected the time that energy balance transitioned from positive to negative values. Then, we calculated the net energy for ice melt one hour before/after the energy balance became negative, assuming that all the negative energy could be used for refreezing, but only in the first hour with energy balance, when there would still be water at the cliff's surface. These results were used to estimate the negative energy flux available for daily refreezing (Q_{rf}; W m^{-1}) and are summarised in Table S7. The relative contribution of refreezing was significant during the winter season. When refreezing was taken into account, the amount of ice cliff melt in December was suppressed by 18.5% (Table S7). However, the contribution of refreezing is small in terms of ice cliff volume loss because of the low ice cliff volume losses observed during the winter season (Fig. 6). From June to September, the mean hourly energy flux does not become negative, and no refreezing is expected. When cumulative Q_{rf} is compared to the cumulative Q_m, its annual melt suppression effect (ice replenishment) was counted as less than 1% of total ice cliff melt (Table S7). Although the year-round scale contribution of refreezing was estimated to be close to negligible, the processes of meltwater discharge and water retention on ice cliff slopes are so complex that more observation and quantification of this component might be required for future development of the dynamic cliff backwasting model.

Although we identified a clear aspect dependence of ice cliff melt rate at Trakarding Glacier, there are cases in other regions where no aspect dependence has been observed. Anderson et al. (2021a) conducted in-situ measurements of ice cliff backwasting rates and found no aspect dependence at debris-covered Kennicott Glacier in Alaska. Hence, those authors concluded that a simple degree-day factor approach could be applied to estimate cliff mass loss across the entire glacier. It would be valuable to apply our approach to other glaciers/regions in order to understand such regional differences in the cliff melt process.

5. Conclusion

This study presented an application of a process-based dynamic ice cliff backwasting model for Trakarding Glacier in the eastern Nepal Himalaya. The study represents the first attempt to estimate full-year-scale cliff mass loss using high-resolution photogrammetry-based terrain data, cliff inventory, and cliff geometry updates. The main conclusions can be summarised as follows:

1. Variations in ice cliff melt rate are more strongly influenced by aspect than by elevation, and the melt rate of south-facing ice cliffs is ∼2 times higher than the rate of north-facing ice cliffs. However, the predominance of north-facing cliffs results in that these cliffs still account for the majority of ice cliff melt.
2. Between July and September, diffuse shortwave radiation accounted for more than 50% of incoming shortwave radiation to ice cliff surfaces. The amount of shortwave radiation flux is strongly dependent on ice cliff aspect with seasonal variability. During the winter season, the direct shortwave radiation of south-facing ice cliffs reached 4.5 times that of north-facing ice cliffs.
3. The aspect dependence of ice cliff melt rate increased during the cold season, but there was no significant aspect-related dependence during the monsoon season. Such seasonal changes are ascribed to changes in solar altitude and monsoonal cloud cover, which are strongly related to direct shortwave radiation to the cliff surface.
4. Although ice cliffs cover less than 2% of the glacier surface, they account for ∼26% of the glacier surface mass loss on the entirety of Trakarding Glacier. Even at the scale of the Trambau–Trakarding glacier system, ice cliffs are a non-negligible melt component, accounting for >7% of the total mass loss of the system, despite occupying <1% of the surface area.

Author contributions. YS, PB, MK, ESM, FP, and KF designed this study. YS, SS, TRG, AS, and KF conducted the field observations. YS analyzed the remote-sensing data. PB and MK provided the ice cliff energy balance model and helped apply it. YS, SS, and KF analyzed meteorological and debris temperature data. YS, PB, MK, ESM, and FK wrote the manuscript. All of the authors contributed to the discussion.

Competing interests. The contact author has declared that neither they nor their co-authors have any competing interests.

References

Anderson LS, Armstrong WH, Anderson RS and Buri P (2021a) Debris cover and the thinning of Kennicott Glacier, Alaska: In situ measurements, automated ice cliff delineation and distributed melt estimates. *The Cryosphere* **15**(1), 265–282. doi: 10.5194/tc-15-265-2021

Anderson LS, Armstrong WH, Anderson RS, Scherler D and Petersen E (2021b) The causes of debris-covered glacier thinning: Evidence for the importance of ice dynamics from Kennicott Glacier, Alaska. *Frontiers in Earth Science* **9**, 680995. doi: 10.3389/feart.2021.680995

Brun F (2019) Heterogeneous influence of glacier morphology on the mass balance variability in high mountain Asia. *Journal of Geophysical Research: Earth Surface* **124**(6), 1331–1345. doi: 10.1029/2018jf004838

Brun F and 9 others (2016) Quantifying volume loss from ice cliffs on debris-covered glaciers using high-resolution terrestrial and aerial photogrammetry. *Journal of Glaciology* 62(234), 684–695. doi:10.1017/jog.2016.54.

Brun F, Berthier E, Wagnon P, Kääb A and Treichler D (2017) A spatially resolved estimate of High Mountain Asia glacier mass balances, 2000-2016. *Nature Geoscience* **10**(9), 668–673. doi: 10.1038/NGEO2999

Brun F and 9 others (2018) Ice cliff contribution to the tongue-wide ablation of Changri Nup Glacier, Nepal, central Himalaya. *The Cryosphere* **12**(11), 3439–3457. doi: 10.5194/tc-12-3439-2018

Buri P, Miles ES, Steiner JF, Immerzeel WW, Wagnon P and Pellicciotti F (2016b) A physically based 3-D model of ice cliff evolution over debris-covered glaciers. *Journal of Geophysical Research: Earth Surface* **121**, 2471–2493. doi: 10.1002/2016JF004039

Buri P, Miles ES, Steiner JF, Ragettli S and Pellicciotti F (2021) Supraglacial ice cliffs can substantially increase the mass loss of debris-covered glaciers. *Geophysical Research Letters* **48**(6). doi: 10.1029/2020gl092150

Buri P and Pellicciotti F (2018) Aspect controls the survival of ice cliffs on debris-covered glaciers. *Proceedings of the National Academy of Sciences of the United States of America.* **115**(17), 4369–4374. doi: 10.1073/pnas.1713892115

Buri P, Pellicciotti F, Steiner JF, Miles ES and Immerzeel WW (2016a) A grid-based model of backwasting of supraglacial ice cliffs on debris-covered glaciers. *Annals of Glaciology* **57**(71), 199–211. doi: 10.3189/2016AoG71A059

Collier E, Maussion F, Nicholson LI, Mölg T, Immerzeel WW and Bush ABG (2015) Impact of debris cover on glacier ablation and atmosphere–glacier feedbacks in the Karakoram. *The Cryosphere* **9**(4), 1617–1632. doi: 10.5194/tc-9-1617-2015

Cooper PI (1969) The absorption of radiation in solar stills. *Solar Energy* **12**(3), 333–346. doi: 10.1016/0038-092X(69)90047-4

Farinotti D and 6 others (2019) A consensus estimate for the ice thickness distribution of all glaciers on Earth. *Nature Geoscience* **12**(3), 168–173. doi: 10.1038/s41561-019-0300-3

Foster LA, Brock BW, Cutler MEJ and Diotri F (2012) A physically based method for estimating supraglacial debris thickness from thermal band remote-sensing data. *Journal of Glaciology* **58**(210), 677–691. doi: 10.3189/2012JoG11J194

Fujita K, Sunako S and Sakai A (2021) *Meteorological Observations at Trakarding Glacier Automatic Weather Station*. Rowaling: Nepal. 2016–2019.

Fyffe CL and 6 others (2014) A distributed energy-balance melt model of an alpine debris-covered glacier. *Journal of Glaciology* **60**(221), 587–602. doi: 10.3189/2014JoG13J148

Fyffe CL, Woodget AS, Kirkbride MP, Deline P, Westoby MJ and Brock BW (2020) Processes at the margins of supraglacial debris cover: Quantifying dirty ice ablation and debris redistribution. *Earth Surface Processes and Landforms* **45**(10), 2272–2290. doi: 10.1002/esp.4879

Girona-Mata M, Miles ES, Ragettli S and Pellicciotti F (2019) High-resolution snowline delineation from Landsat imagery to infer snow cover controls in a Himalayan catchment. *Water Resources Research* **55**, 6754–6772. doi: 10.1029/2019WR024935

Han H, Wang J, Wei J and Liu S (2010) Backwasting rate on debris-covered Koxkar glacier, Tuomuer mountain, China. *Journal of Glaciology* **56**(196), 287–296. doi: 10.3189/002214310791968430

Herreid S and Pellicciotti F (2020) The state of rock debris covering Earth's glaciers. *Nature Geoscience* **13**(9), 621–627. doi: 10.1038/s41561-020-0615-0

Heynen M, Miles E, Ragettli S, Buri P, Immerzeel WW and Pellicciotti F (2016) Air temperature variability in a high-elevation Himalayan catchment. *Annals of Glaciology* **57**(71), 212–222. doi: 10.3189/2016AoG71A076

Hugonnet R and 10 others (2021) Accelerated global glacier mass loss in the early twenty-first century. *Nature* **592**(7856), 726–731. doi: 10.1038/s41586-021-03436-z

Huss M (2013) Density assumptions for converting geodetic glacier volume change to mass change. *The Cryosphere* **7**(3), 877–887. doi: 10.5194/tc-7-877-2013

Immerzeel WW and 6 others (2014) High-resolution monitoring of Himalayan glacier dynamics using unmanned aerial vehicles. *Remote Sensing of Environment* **150**, 93–103. doi: 10.1016/j.rse.2014.04.025

Kneib M and 9 others (2020) Mapping ice cliffs on debris-covered glaciers using multispectral satellite images. *Remote Sensing of Environment* **253**, 112201. doi: 10.1016/j.rse.2020.112201

Kneib M and 6 others (2021) Interannual Dynamics of Ice Cliff Populations on Debris-Covered Glaciers From Remote Sensing Observations and Stochastic Modeling. *Journal of Geophysical Research: Earth Surface* **126**(10), e2021JF006179. doi: 10.1029/2021JF006179

Kneib M and 10 others (2022) Sub-seasonal variability of supraglacial ice cliff melt rates and associated processes from time-lapse photogrammetry. *The Cryosphere* **16**(11), 4701–4725. doi: 10.5194/tc-16-4701-2022

Kneib M and 13 others (2023) Controls on Ice Cliff Distribution and Characteristics on Debris-Covered Glaciers. *Geophysical Research Letters* **50**(6), e2022GL102444. doi: 10.1029/2022GL102444

Kraaijenbrink PDA, Shea JM, Pellicciotti F, de JSM and Immerzeel WW (2016) Object-based analysis of unmanned aerial vehicle imagery to map and characterize surface features on a debris-covered glacier. *Remote Sensing of Environment* **186**, 581–595. doi: 10.1016/j.rse.2016.09.013

Kraaijenbrink PDA and 6 others (2018) Mapping surface temperatures on a debris-covered glacier with an unmanned aerial vehicle. *Frontiers in Earth Science* **6**, 64. doi: 10.3389/feart.2018.00064

Lamsal D, Fujita K and Sakai A (2017) Surface lowering of the debris-covered area of Kanchenjunga Glacier in the eastern Nepal Himalaya since 1975, as revealed by Hexagon KH-9 and ALOS satellite observations. *The Cryosphere* **11**(6), 2815–2827. doi: 10.5194/tc-11-2815-2017

Miles ES and 6 others (2017) Pond dynamics and supraglacial-englacial connectivity on debris-covered Lirung glacier, Nepal. *Frontiers in. Earth Science* **5**, 69. doi: 10.3389/feart.2017.00069

Miles ES, Willis I, Buri P, Steiner JF, Arnold NS and Pellicciotti F (2018) Surface Pond Energy Absorption Across Four Himalayan Glaciers Accounts for 1/8 of Total Catchment Ice Loss. *Geophysical Research Letters* **45**(19), 10464–10473. doi: 10.1029/2018GL079678

Miles E, McCarthy M, Dehecq A, Kneib M, Fugger S and Pellicciotti F (2021) Health and sustainability of glaciers in High Mountain Asia. *Nature Communications* **12**(1), 2868. doi: 10.1038/s41467-021-23073-4

Miles ES, Steiner JF, Buri P, Immerzeel WW and Pellicciotti F (2022) Controls on the relative melt rates of debris-covered glacier surfaces. *Environmental Research Letters* **17**(6), 064004. doi: 10.1088/1748-9326/ac6966

Mishra NB and 6 others (2022) Quantifying heterogeneous monsoonal melt on a debris-covered glacier in Nepal Himalaya using repeat uncrewed aerial system (UAS) photogrammetry. *Journal of Glaciology* **68**(268), 288–304. doi: 10.1017/jog.2021.96

Moore PL (2018) Stability of supraglacial debris. *Earth Surface Processes and Landforms* **43**(1), 285–297. doi: 10.1002/esp.4244

Nuimura T, Fujita K, Fukui K, Asahi K, Aryal R and Ageta Y (2011) Temporal Changes in Elevation of the Debris-Covered Ablation Area of Khumbu Glacier in the Nepal Himalaya since 1978. *Arctic, Antarctic, and Alpine Research* **43**(2), 246–255. doi: 10.1657/1938-4246-43.2.246

Nuimura T, Fujita K, Yamaguchi S and Sharma RR (2012) Elevation changes of glaciers revealed by multitemporal digital elevation models calibrated by GPS survey in the Khumbu region, Nepal Himalaya, 1992–2008. *Journal of Glaciology* **58**(210), 648–656. doi: 10.3189/2012JoG11J061

Nuimura T and 12 others (2015) The GAMDAM glacier inventory: A quality-controlled inventory of Asian glaciers. *The Cryosphere* **9**(3), 849–864. doi: 10.5194/tc-9-849-2015

Østrem G (1959) Ice melting under a thin layer of moraine, and the existence of ice cores in moraine ridges. *Geografiska Annaler* **41**(4), 228–230.

Pellicciotti F, Stephan C, Miles E, Herreid S, Immerzeel WW and Bolch T (2015) Mass-balance changes of the debris-covered glaciers in the Langtang Himal, Nepal, from 1974 to 1999. *Journal of Glaciology* **61**(226), 373–386. doi: 10.3189/2015JoG13J237

Petersen E, Hock R and Loso MG (2024) Stream hydrology controls on ice cliff evolution and survival on debris-covered glaciers. *Earth Surface Dynamics* **12**, 727–745. doi: 10.5194/esurf-12-727-2024

Reid TD and Brock BW (2014) Assessing ice-cliff backwasting and its contribution to total ablation of debris-covered Miage glacier, Mont Blanc massif, Italy. *Journal of Glaciology* **60**(219), 3–13. doi: 10.3189/2014JoG13J045

Reindl DT, Beckman WA and Duffie JA (1990) Diffuse fraction correlations. *Solar Energy* **45**(1), 1–7. doi: 10.1016/0038-092x.(90)90060-p

Rounce DR and 10 others (2021) Distributed Global Debris Thickness Estimates Reveal Debris Significantly Impacts Glacier Mass Balance. *Geophysical Research Letters* **48**(8), e2020GL091311. doi: 10.1029/2020GL091311

Sakai A (2019) Brief communication: Updated GAMDAM glacier inventory over high-mountain Asia. *The Cryosphere* **13**(7), 2043–2049. doi: 10.5194/tc-13-2043-2019

Sakai A, Nakawo M and Fujita K (1998) Melt Rate of Ice Cliffs on the Lirung Glacier, Nepal Himalayas, 1996. *Bulletin of Glaciological Research* **16**, 57–66.

Sakai A, Nakawo M and Fujita K (2002) Distribution characteristics and energy balance of ice cliffs on debris-covered glaciers, Nepal Himalaya. *Arctic, Antarctic, and Alpine*. *Research* **34**(1), 12. doi: 10.2307/1552503

Salerno F and 6 others (2017) Debris-covered glacier anomaly? Morphological factors controlling changes in the mass balance, surface area, terminus position, and snow line altitude of Himalayan glaciers. *Earth and Planetary Science Letters* **471**, 19–31. doi: 10.1016/j.epsl.2017.04.039

Sato Y, Fujita K, Inoue H, Sakai A and Karma (2022) Land- to lake-terminating transition triggers dynamic thinning of a Bhutanese glacier. *The Cryosphere* **16**(6), 2643–2654. doi: 10.5194/tc-16-2643-2022

Sato Y and 8 others (2021) Ice Cliff Dynamics of Debris-Covered Trakarding Glacier in the Rolwaling Region, Nepal Himalaya. *Frontiers in Earth Science* **9**, 623623. doi: 10.3389/feart.2021.623623

Shean DE, Bhushan S, Montesano P, Rounce DR, Arendt A and Osmanoglu B (2020) A Systematic, Regional Assessment of High Mountain Asia Glacier Mass Balance. *Frontiers in Earth Science* **7**, 363. doi: 10.3389/feart.2019.00363

Steiner JF, Pellicciotti F, Buri P, Miles ES, Immerzeel WW and Reid TD (2015) Modelling ice-cliff backwasting on a debris-covered glacier in the Nepalese Himalaya. *Journal of Glaciology* **61**(229), 889–907. doi: 10.3189/2015JoG14J194

Steiner JF and Pellicciotti F (2016) Variability of air temperature over a debris-covered glacier in the Nepalese Himalaya. *Annals of Glaciology* **57**(71), 295–307. doi: 10.3189/2016AoG71A066

Steiner JF, Buri P, Miles ES, Ragettli S and Pellicciotti F (2019) Supraglacial ice cliffs and ponds on debris-covered glaciers: Spatio-temporal distribution and characteristics. *Journal of Glaciology* **65**(252), 617–632. doi: 10.1017/jog.2019.40

Sunako S, Fujita K, Sakai A and Kayastha RB (2019) Mass balance of Trambau Glacier, Rolwaling region, Nepal Himalaya: In-situ observations, long-term reconstruction and mass-balance sensitivity. *Journal of Glaciology* **65**, 605–616.

Watson CS, Quincey DJ, Carrivick JL and Smith MW (2017b) Ice cliff dynamics in the Everest region of the Central Himalaya. *Geomorphology* **278**, 238–251.

Watson CS, Quincey DJ, Smith MW, Carrivick JL, Rowan AV and James MR (2017a) Quantifying Ice Cliff Evolution with Multi-Temporal Point Clouds on the Debris-Covered Khumbu Glacier, Nepal. *Journal of Glaciology* **63**(241), 823–837. doi: 10.1017/jog.2017.47

Wei J and 7 others (2021) Longbasaba Glacier recession and contribution to its proglacial lake volume between 1988 and 2018. *Journal of Glaciology*, **67**(263), 473–484. 10.1017/jog.2020.119

Westoby MJ and 6 others (2020) Geomorphological evolution of a debris-covered glacier surface. *Earth Surface Processes and Landforms* **45**(14), 3431–3448. doi: 10.1002/esp.4973

Zhao C and 7 others (2023) Thinning and surface mass balance patterns of two neighbouring debris-covered glaciers in the southeastern Tibetan Plateau. *The Cryosphere* **17**(9), 3895–3913. doi: 10.5194/tc-17-3895-2023

Modelling seasonal fluctuations and aspect characteristics of ice-cliff melt on the debris-covered Trakarding Glacier, Rolwaling Valley, Nepal Himalaya

Yota Sato*[1, 2], Pascal Buri[3, 4], Marin Kneib[3, 5,], Evan S. Miles[3], Sojiro Sunako[6], Tika R. Gurung[7], Akiko Sakai[2], Francesca Pellicciotti[3, 8], Koji Fujita[2]

[1] Japan Agency for Marine-Earth Science and Technology (JAMSTEC), Yokohama, Japan
[2] Graduate School of Environmental Studies, Nagoya University, Nagoya, Japan
[3] Swiss Federal Institute for Forest, Snow and Landscape Research (WSL), Birmensdorf, Switzerland
[4] Geophysical Institute, University of Alaska Fairbanks, Fairbanks, USA
[5] Institute of Environmental Engineering, ETH Zurich, Zurich, Switzerland
[6] Snow and Ice Research Center, National Research Institute for Earth Science and Disaster Resilience (NIED), Nagaoka, Japan
[7] International Center for Integrated Mountain Development (ICIMOD), Kathmandu, Nepal
[8] Department of Geography, Northumbria University, Newcastle, UK
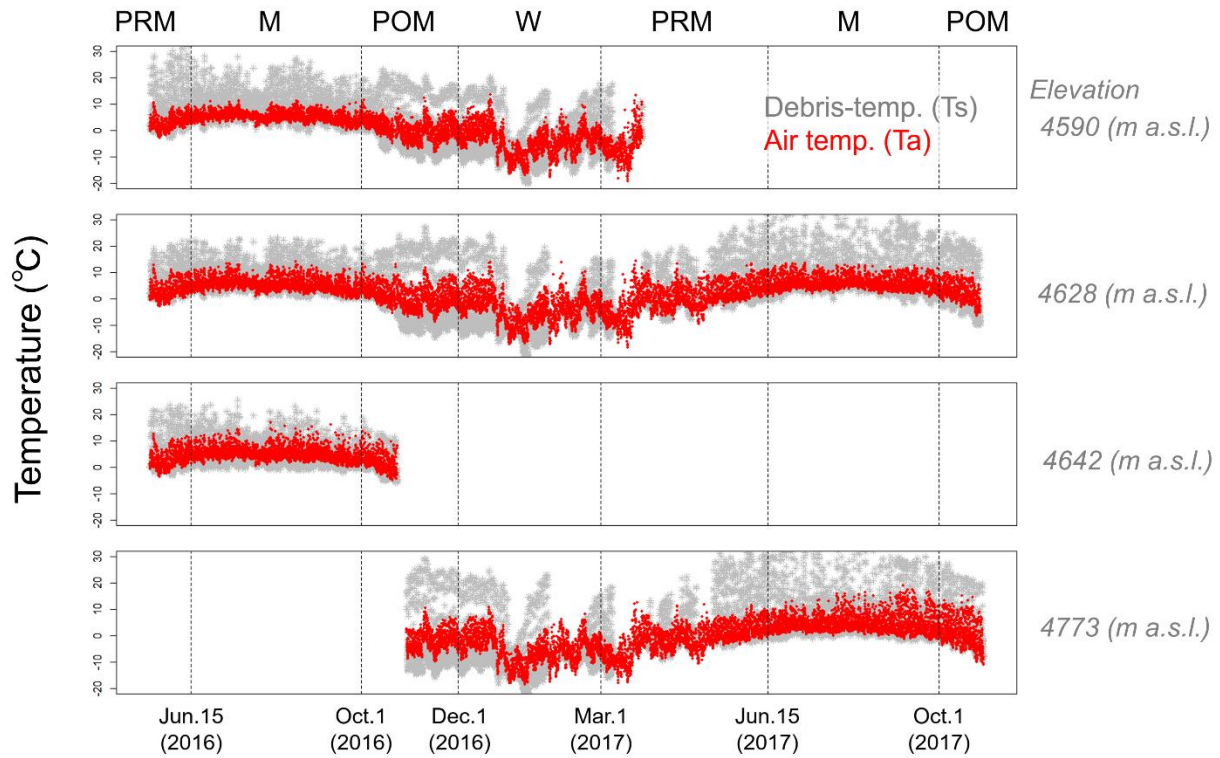
Fig. S1. Debris surface temperature (T_s) and air temperature (T_a). The locations of the T_a and T_s temperature sensors are shown in **Figure 1d**.

Fig. S2. Time-lapse photographs taken near the terminus. These examples were taken at 13:46 (in Nepal time) on **(a)** 15 January, **(b)** 15 February, **(c)** 15 March, and **(d)** 15 April 2019. Photographs **(b)**, **(c)**, and **(d)** were classified as days with snow cover.
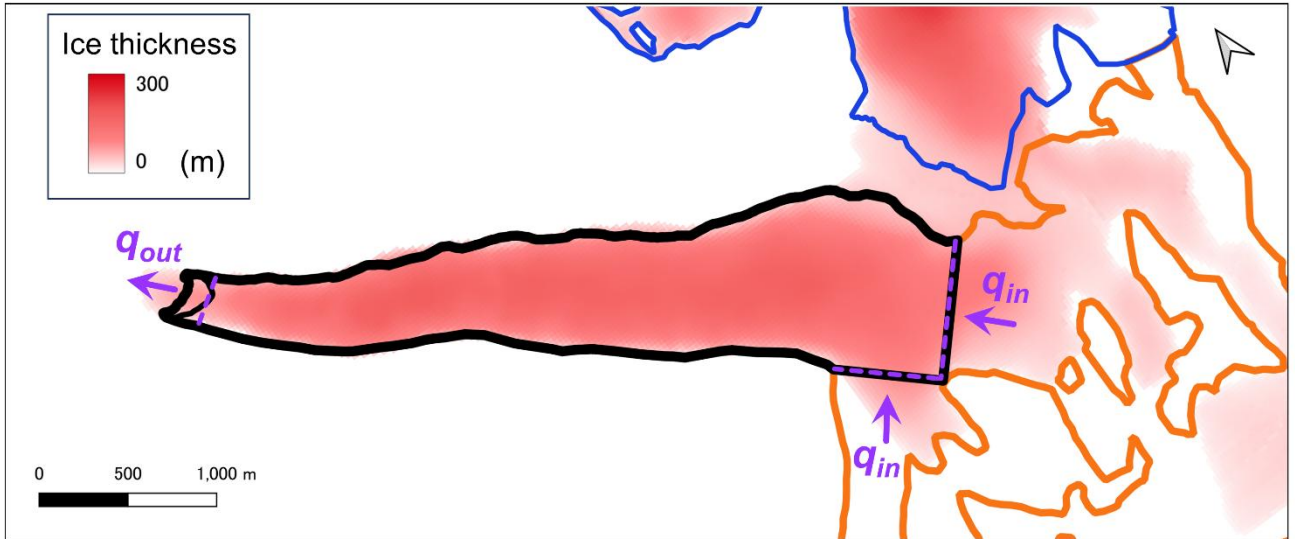
Fig. S3. Ice thickness distribution of Trakarding Glacier (Farinotti and others, 2019). Dashed purple lines represent upper/lower ice flux gates for calculating the mass balance of the debris-cvered tongue as an ablation zone. The term q_{in}/q_{out} denotes incoming/outgoing ice fluxes.
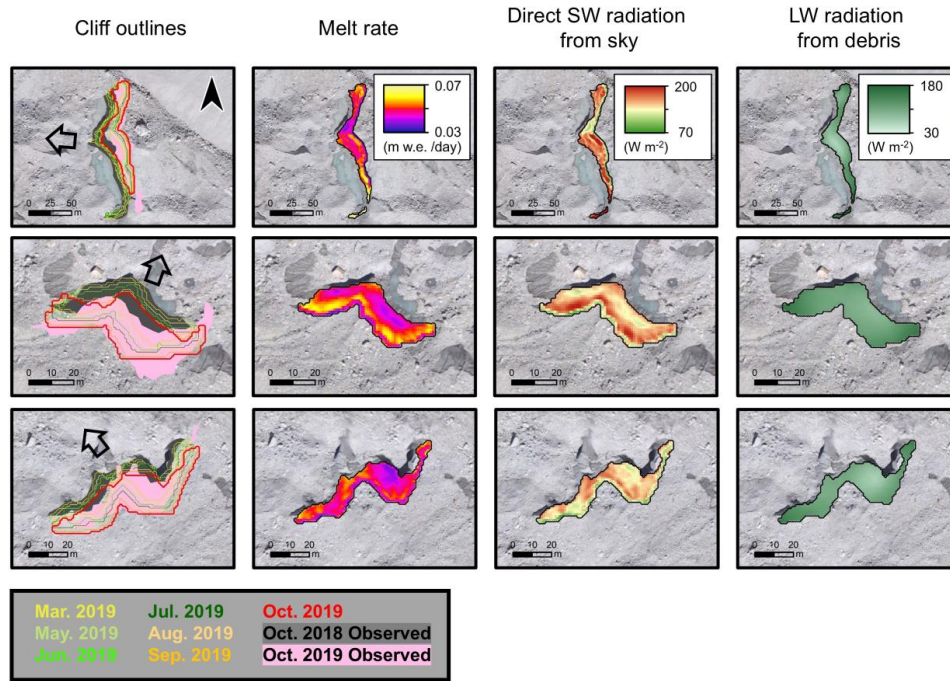
Fig. S4. Examples of cliff backwasting model output. The melt rate, direct shortwave radiation from the sky, and longwave radiation from the surrounding debris are monthly averaged values for May 2019. Arrows in the left panels represent cliff aspects.
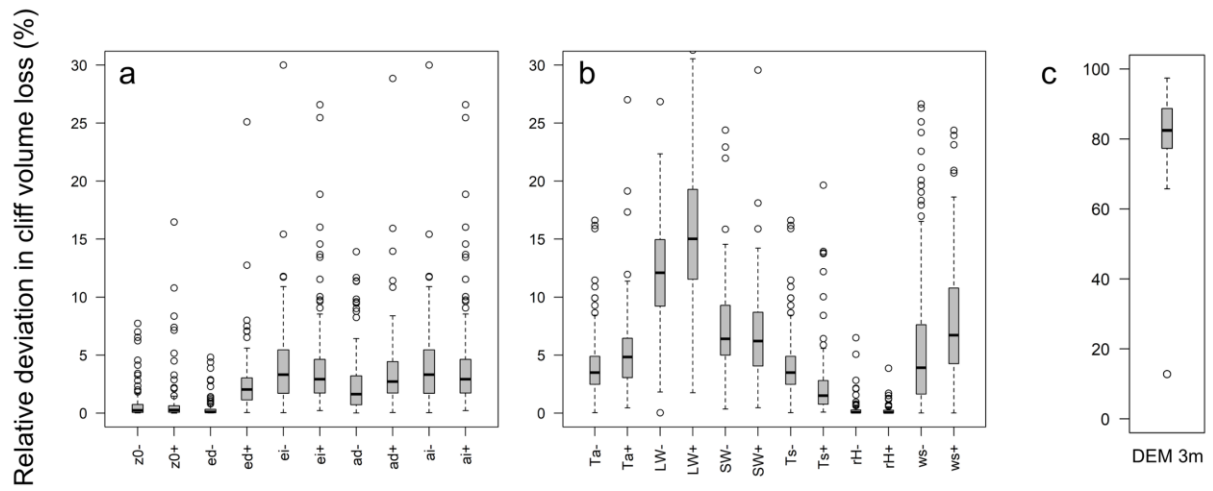
Fig. S5. Sensitivity analysis for **(a)** five physical parameters, **(b)** six meteorological parameters, and **(c)** DEM resolution (3.0 m). The '+/−' in the x-axis labels indicates the upper/lower bounds of each parameter. Grey boxes show the 25–75th percentile, horizontal black lines in the boxes represent medians, and blank plots depict outliers. The ranges of sensitivity analysis were taken from Buri and others (2021) and are presented in **Table S2**.
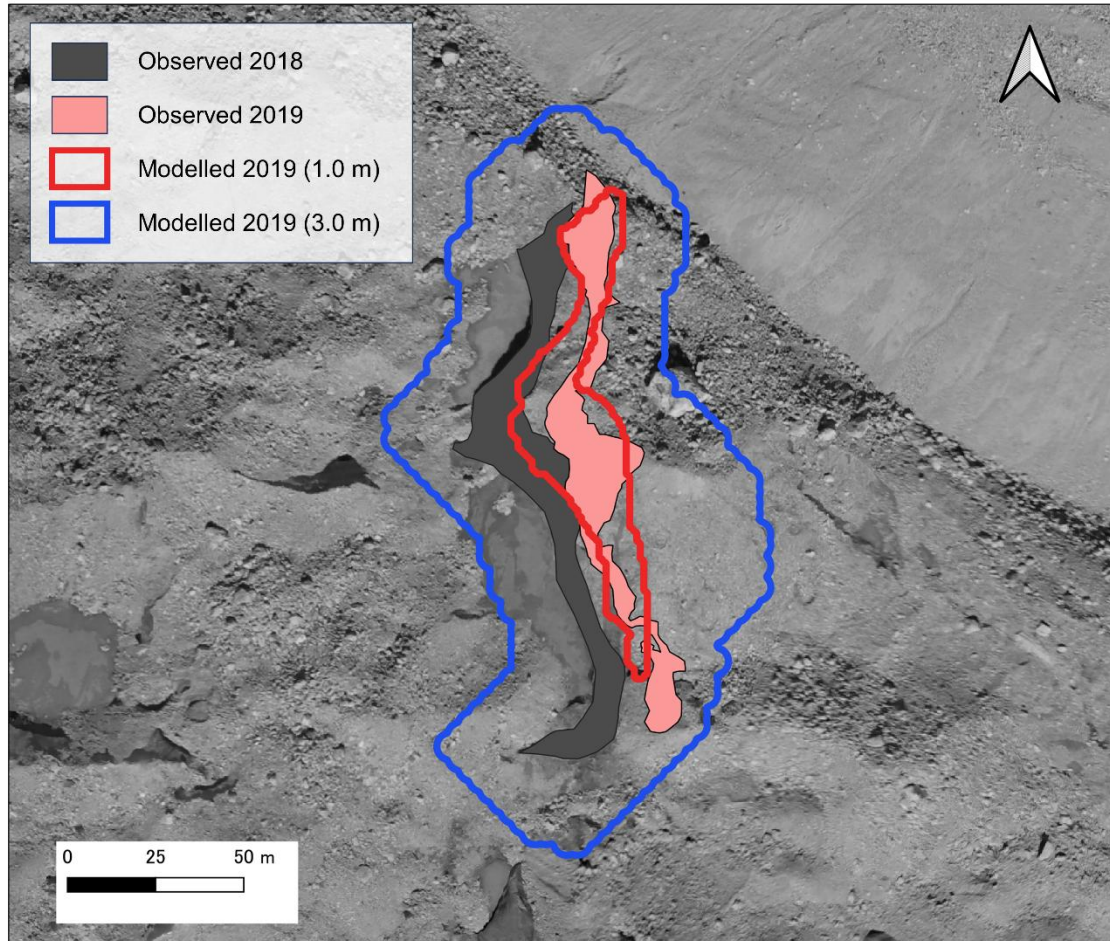
Fig. S6. Example of sensitivity analysis for DEM resolution. The red outline indicates the original output with the base setting (1.0 m resolution DEM), and the blue outline represents simulation with a 3.0 m resolution DEM.
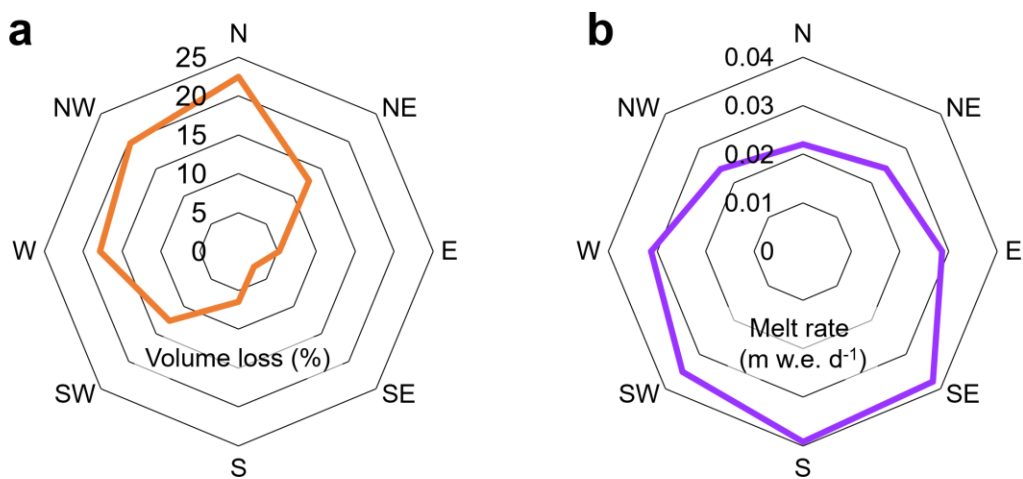
Fig. S7. Aspect distribution of **(a)** relative ice cliff volume loss to total ice cliff volume loss and **(b)** mean ice cliff melt rate from October 2018 to October 2019.
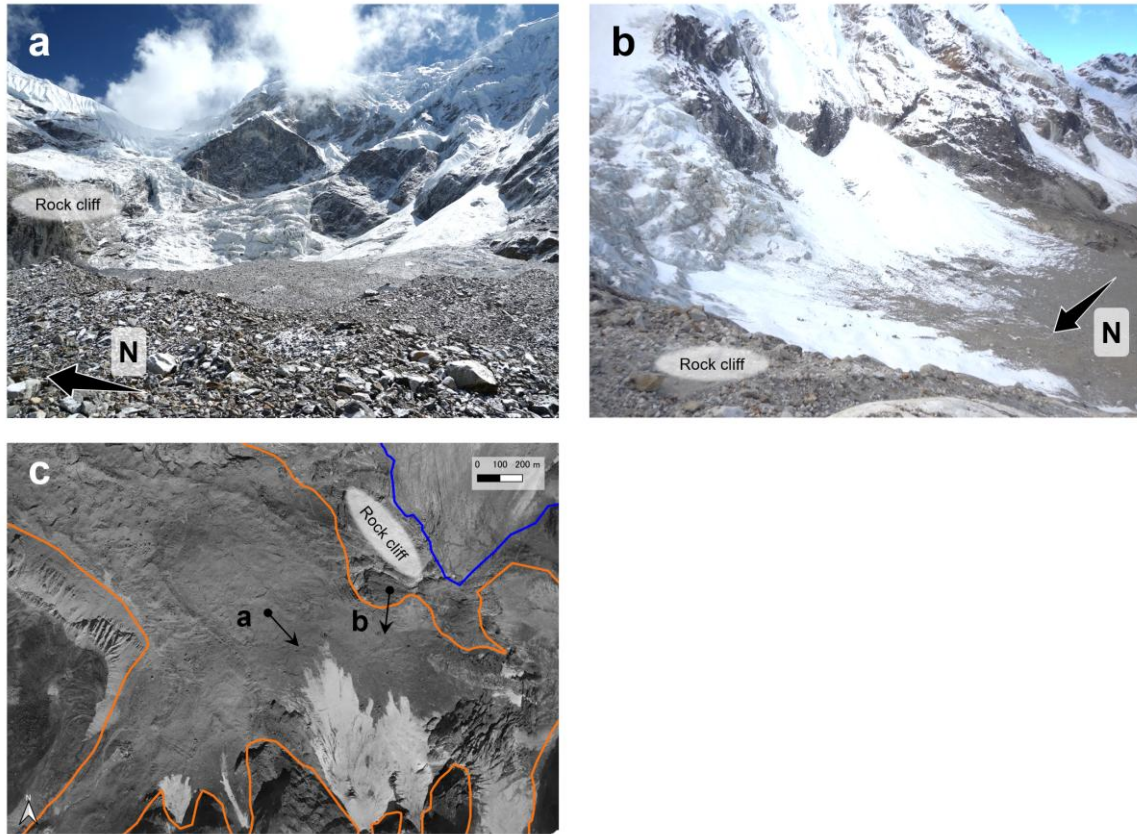
Fig. S8. Upper part of Trakarding Glacier; **(a)** and **(b)** are terrestrial photographs, and **(c)** is a map of the upper part of the glacier. Arrows in panel **(c)** show the directions/locations from which the photographs were taken.
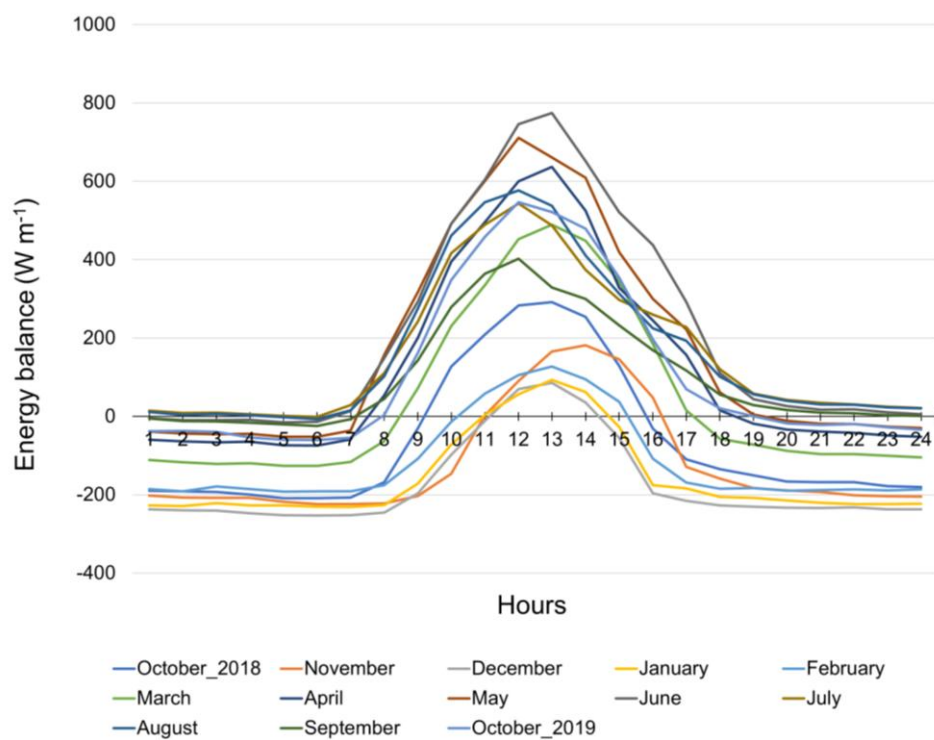
Fig S9. Diurnal changes of energy balance. The flux values are averaged across all ice cliff surfaces.

9

Table S1. Model parameters and settings. Thresholds for slope and debris view factor were tuned for the 1.0 m resolution used in this study (Section 2.4).

Parameter	Setting or Threshold	Source
Debris albedo	0.15	Steiner and others (2015)
Ice albedo	0.20	Steiner and others (2015)
Emissivity of debris	0.93	Steiner and others (2015)
Emissivity of ice	0.97	Steiner and others (2015)
Pond effect beside cliff (m d^{-1})	0.033	Miles and others (2016)
Surface roughness length (m)	0.002	Steiner and others (2015)
Slope threshold (°)	35	This study
Threshold for debris view factor	0.6	This study
Resolution of DEM (m^2)	1.0	This study

Table S2. Parameters used in the sensitivity analysis. Upper/lower values are from Buri and others (2021).

	Parameter	Central value	Changed value (upper/lower)
Physical parameters	Surface roughness (z0)	0.002	0.0001/0.01
	Emissivity of debris (ed)	0.93	0.931/0.965 (±20%)
	Emissivity of ice (ei)	0.97	0.951/0.989 (±20%)
	Debris albedo (ad)	0.15	0.12/0.18 (±20%)
	Ice albedo (ai)	0.2	0.16/0.24 (±20%)
Meteorological parameters	Air temperature (Ta)	-	−2K/+2K
	Incoming longwave radiation (LW)	-	−30 W m^{-2}/+30 W m^{-2}
	Incoming shortwave radiation (SW)	-	−50 W m^{-2} / +50 W m^{-2}
	Debris surface temperature (Ts)	-	−2K/+2K
	Relative humidity (rH)	-	−20%/+20%
	Wind speed (ws)	-	×0.5/×2.0

Table S3. Summary of monthly ice cliff melt rate listed over time with respect to ice cliff aspect (**Fig. 9**).

	Melt rate (m w.e. d^{-1})				
	All-aspect	**North**	**East**	**South**	**West**
Oct. 2018	0.016	0.009	0.020	0.036	0.024
Nov. 2018	0.008	0.003	0.011	0.027	0.016
Dec. 2018	0.003	0.001	0.006	0.019	0.010
Jan. 2019	0.004	0.001	0.006	0.018	0.010
Feb. 2019	0.009	0.004	0.009	0.018	0.013
Mar. 2019	0.032	0.025	0.032	0.042	0.039
Apr. 2019	0.045	0.041	0.046	0.051	0.048
May. 2019	0.056	0.055	0.058	0.057	0.057
Jun. 2019	0.065	0.065	0.064	0.062	0.066
Jul. 2019	0.049	0.049	0.050	0.046	0.048
Aug. 2019	0.050	0.049	0.054	0.050	0.050
Sep. 2019	0.032	0.031	0.035	0.035	0.033
Oct. 2019	0.039	0.032	0.045	0.052	0.044

Table S4. Mean annual energy flux for ice cliffs of Trakarding Glacier. All units are in W m^{-2}. The mean energy fluxes are summarised in all ice cliffs (left column), only north-facing ice cliffs (center column) and only south-facing ice cliffs (right column). Values in brackets are the percentages of components of incoming shortwave radiation (I_s, D_s, and D_t) and incoming longwave radiation (L_s and L_d).

	All aspects	North-facing	South-facing
I_s	89.7 (55.0)	71.0 (48.9)	133.3 (64.5)
D_s	62.8 (38.5)	62.5 (43.6)	62.5 (30.3)
D_t	10.7 (6.6)	10.8 (7.5)	10.8 (5.2)
I_r	−32.6	−28.7	−41.3
L_s	135.1 (57.0)	137.0 (57.6)	131.4 (57.9)
L_d	102.0 (43.0)	100.7 (42.4)	95.7 (42.1)
L_o	−306.2	−306.2	−306.2
H	−0.4	−0.5	0.1
LE	−25.8	−25.9	−25.5
Q_m	95.5	76.0	137.9

Table S5. Mean and standard deviation of annual meteorological components observed at the AWS.

$T_{a, AWS}$ (°C)		$SW_{in, AWS}$ (W m^{-2})		Clearness index	
Mean	**SD**	**Mean**	**SD**	**Mean**	**SD**
−1.3	4.9	559.2	113.7	0.6	0.1

Table S6. Disappearing ice cliffs (i.e., ice cliffs buried by debris) detected by observations and as simulated in the dynamic cliff backwasting model. Data for observed disappearing/surviving ice cliffs are from Sato and others (2021).

		Observation	
		Disappearing	**Surviving**
Model	**Disappearing**	55	16
	Surviving	161	223

Table S7. Summary of refreezing estimation. Q_{rf} is the negative heat for providing refreezing. The snow cover days were excluded from Q_{rf} analysis.

Month	Starting hour of negative energy balance	Q_{rf} $(W\,m^{-2})$	Relative Q_{rf} to total Q_m (%)
October 2018	15:00-16:00	31.4	2.4
November	16:00-17:00	48.1	7.6
December	14:00-15:00	35.2	18.5
January	14:00-15:00	26.7	12.4
February	15:00-16:00	37.3	8.8
March	17:00-18:00	15.2	0.6
April	18:00-19:00	15.7	0.4
May	19:00-20:00	4.4	0.1
June	-	-	-
July	-	-	-
August	-	-	-
September	-	-	-
October 2019	19:00-20:00	0.6	0.2×10^{-1}

REFERENCES

Buri P, Miles ES, Steiner JF, Ragettli S and Pelliccciotti F (2021) Supraglacial ice cliffs can substantially increase the mass loss of debris-covered glaciers. *Geophysical Research Letters* **48**(6). doi:10.1029/2020gl092150.

Farinotti D and 6 others (2019) A consensus estimate for the ice thickness distribution of all glaciers on Earth. *Nature Geoscience* **12**(3), 168–173. doi:10.1038/s41561-019-0300-3.

Miles ES, Pelliccciotti F, Willis IC, Steiner JF, Buri P and Arnold NS (2016) Refined energy-balance modelling of a supraglacial pond, Langtang Khola, Nepal. *Annals of Glaciology* **57**(71), 29–40. doi:10.3189/2016AoG71A421.

Sato Y and 8 others (2021) Ice Cliff Dynamics of Debris-Covered Trakarding Glacier in the Rolwaling Region, Nepal Himalaya. *Frontiers in Earth Science* **9**, 623623. doi:10.3389/feart.2021.623623.

Steiner JF, Pelliccciotti F, Buri P, Miles ES, Immerzeel WW and Reid TD (2015) Modelling ice-cliff backwasting on a debris-covered glacier in the Nepalese Himalaya. *Journal of Glaciology* **61**(229), 889–907. doi:10.3189/2015JoG14J194.